1 The impact of tropical cyclones on regional ozone

2 pollution and its future trend in the Yangtze River Delta

- 3 of China
- 4 Mengzhu Xi¹, Min Xie^{1, 2*}, Da Gao^{2, #}, Danyang Ma¹, Yi Luo^{2, 33}, Danyang Ma¹,
- 5 Lingyun Feng¹, Shitong Chen¹, Shuxian Zhang¹
- 6 School of Environment, Nanjing Normal University, Nanjing 210023, China
- 7 ² Carbon monitoring and digital application technology center, Carbon peak and carbon neutralization
- 8 strategy institute of Jiangsu Province, Nanjing 210023, ChinaSchool of Atmospheric Science, Nanjing
- 9 <u>University, Nanjing 210023, China</u>

10

- 11 3-3 Ningbo Ecological Environment Monitoring Center of Zhejiang Province, Ningbo 315048, China_
- 12 ** Now at Center for Aerosol Science and Engineering, Department of Energy, Environmental and
- 13 <u>Chemical Engineering, Washington University in St. Louis, St. Louis, MO, USA</u>
- 14 Correspondence to: Min Xie (minxie@njnu.edu.cn) and Danyang Ma (dyma@njnu.edu.cn)
- 15 Abstract: Tropical cyclones (TCs) have a significant impact on ozone (O₃) in coastal regions by affecting 16 atmospheric circulation and meteorological conditions. This paper investigates the impact and its future 17 changing trends in the Yangtze River Delta (YRD) region. It was found that regional O₃ pollution usually 18 occurred before TCs made landfall and after they dissipated in 2018-2022. We classified the weather 19 patterns (SWPs) from June to September during 2018–2022 into four main categories. As pollution levels 20 increase within the TCs weather pattern, regional temperatures rise, relative humidity decreases, and wind speeds weaken, creating a favorable environment for O₃ formation and accumulation. The annual 21 22 O3 concentration series is reconstructed based on changes in SWP frequency and intensity, quantifying 23 the impact of various SWPs on future O₃ variations. The analysis focuses on the number of days with the 24 TCs weather pattern and their contribution to O₃ variation. Under the SSP2-4.5 and SSP5-8.5 scenarios, 25 future YRD O3 concentrations from June to September will increase to varying degrees relative to historical average O₃ concentrations, with average increases of approximately 1.88 μg/m³ and 6.86 μg/m³, 26 27 respectively. Under all future scenarios, the number of days with TC weather pattern increases to varying 28 degrees, and the frequency of TCs increases significantly. The contribution of TCs weather pattern to O₃ 29 changes is increasing compared to the historical period. Using rotation principal component analysis in 30 T mode (PTT) method, five main synoptic weather patterns (SWPs) are identified. The TC weather 31 pattern (SWP5) is a high-frequency weather pattern in summer (72.22%). Subsequently, with the aid of 32 the data reconstruction of O₃ concentrations, how SWPs, especially TCs, affect O₃ is quantified. It is found that the intensity of SWPs is the dominant factor for the annual variation sequence of O₃₅ 33 contributing 81.39% to the change in O₃ annual concentrations. Finally, based on future climate scenario 34 35 data, the changes in TCs and their impact on the trend of O₃ are discussed. Under the SSP2 4.5 scenario, 36 the O₃ in the warm seasons of the YRD is expected to increase by 8.3 µg/m³ compared with the historical 37 period, and the SWP5 is expected to contribute the most to the estimated O₂ concentration in 2030 (15.14%). Under the SSP5 8.5 scenario, the O₃ will increase by 10.9 μg/m³. The SWP5 is expected to 38 39 contribute the most to the estimated O_3 in 2060 (20.66%). This shows that the intensification of climate 40 change will intensify the impact of TCs on O₃ in the YRD, and monitoring and early warning need to be strengthened. 41

1 Introduction

42

43

44

45

46

47 48

49

50

51

52

53 54

55

56 57

58

59

60

61

62

63

64

65

66

67

68

69

70

71

72

73

74

75

76 77

78

79

80

81

82

83

84

In recent years, the concentration of ground-level O₃ in many cities in China has significantly exceeded standards and has intensified. O₃ has replaced Particulate Matter (PM) as the primary pollutant in many regions (Wang et al., 2023b; Yang et al., 2025; Zhao et al., 2020). Ground-level O₃ is mainly generated by photochemical reactions of volatile organic compounds (VOCs) and nitrogen oxides (NO_x) under sunlight (Lu et al., 2019; Zhang et al., 2024). High concentrations of O₃ can damage the human respiratory system, destroy the human immune system, and even increase the risk of death (Gong et al., 2024; Wang et al., 2025). It can also damage the ecosystem, causing plant leaf necrosis and crop yield reduction (Li et al., 2024). In recent years in the YRDIn the past years of YRD, high emissions of motor vehicle and industrial waste gases, coupled with complex terrain and meteorological conditions due to urbanization, have led to complex air pollution characterized by high concentrations of O₃ and PM concentrations (Zhan et al., 2024). According to the 2020 China Ecological Environment Bulletin, in the YRD, the number of days with air quality exceeding the standard with O₃ as the primary pollutant accounted for over 50% of the total number of days exceeding the standard. According to the 2020 China Ecological Environment Bulletin, in many Chinese cities, the number of days with air quality exceeding the standard with O₃ as the primary pollutant accounted for over 50% of the total number of days exceeding the standard.

O₃ concentration is regulated by precursor emissions and meteorological conditions during its generation process (Gong et al., 2022; Xie et al., 2016; Xu et al., 2023b). Meteorological factors such as temperature, humidity, precipitation, atmospheric stability, and mixing layer height play important roles in the emission, transportation, and dispersion, chemical reaction, and dry and wet deposition of air pollutants (Chen et al., 2020; Li et al., 2020). Regional O₃ pollution events are often triggered by meteorological conditions such as strong radiation, high temperature, low relative humidity, and low wind speed (Wang et al., 2024b; Zhan and Xie, 2022). Changes in meteorological conditions are affected by weather systems, and the role of weather systems in O₃ concentrations changes has also received widespread attention.

Tropical cyclone (TC) activities have a profound impact on the ecological environment of China's coastal areas. In the summer and autumn seasons when O₃ pollution is frequent, TCs are one of the key weather systems that induce O₃ pollution in the YRD (Qi et al., 2024; Shu et al., 2016; Zhan and Xie, 2022). Although the strong winds and precipitation brought by landfalling TCs have a strong scavenging effect on pollutants, the peripheral circulation of TCs away from lands will significantly change the temperature field, wind field, and boundary layer structure, thereby affecting the chemical and physical processes related to O₃ generation, transport, dispersion and deposition, which may in turn aggravate O₃ pollution (Chow et al., 2018; Jiang et al., 2015; Lam et al., 2005; Xu et al., 2023a; Yang et al., 2012). Deng et al. (2019) found that under the influence of the peripheral circulation of TCs, the Pearl River Delta (PRD) is prone to high temperature, low humidity, low wind speed, and strong radiation, which leads to the occurrence of high O₃ and PM concentrations. Hu et al. (2023) focused on analyzing the atmospheric processes that are conducive to the increase in O₃ concentration and the continuous exceedance of O₃ during TC activities, and found that the prevailing downdraft over the PRD brought meteorological conditions of clear sky, low wind speed, high boundary layer, and low relative humidity, which led to the continuous excess of O₃ concentration. Wang et al. (2024a) found that the continuous northward TCs produced and maintained meteorological conditions conducive to the generation of O₃, promoted the local accumulation and cross-regional transmission of O₃, and jointly led to a 30.2% increase

86

87

88 89

90

91

92

93

94

95 96

97

98

99

100

101

102

103

104

105

106

107

108

109

110

111

112

113

114

115

116

117

118

119

120

121

122123

124

125

126

127

128

in O₃ concentration in eastern China and a prolonged O₃ pollution period. Xu et al. (2023a) further revealed that when a typhoon landed in the YRD, the contribution of BVOC to O₃ in the Beijing-Tianjin-Hebei region reached 10 ppb; when the TCs moved to Beijing-Tianjin-Hebei region, the cross-transport between the northern China air mass and the YRD contributed half of the O₃ related to biological emissions. The peripheral winds and downdrafts of TCs lead to high temperatures and stable weather, which affect O₃ concentrations by affecting regional transport and biological emissions.

The Sixth Assessment Report of the Intergovernmental Panel on Climate Change (IPCC) has established that the rise in the average surface temperature of the earth, caused by human activities, has become a scientific consensus. The Sixth Assessment Report of the Intergovernmental Panel on Climate Change (IPCC) pointed out that the rise in the average surface temperature of the earth caused by human activities has become a scientific consensus. Compared with the average surface temperature before industrialization (1850 1900), the global average surface temperature rose by about 0.8 1.3 °C due to human activities during 2010-2019 Compared with the average surface temperature before industrialization (1850–1900), the global average surface temperature increased by about 0.8–1.3 °C due to human activities during 2010-2019 (Adak et al., 2023). In the context of global climate change, with the increases in greenhouse gas emissions, global warming, and interannual climate changes, the state of the atmosphere and ocean has changed, and sea-level rise and extreme climate events have occurred frequently, which have a low-frequency modulating effect on TCs (Chu et al., 2020; Moon et al., 2023; Moon et al., 2025; Wang et al., 2023a). In the context of global climate change, with the increases in greenhouse gas emissions, global warming, and interannual climate changes, the state of the atmosphere and ocean has changed, and sea level rise and extreme climate events have occurred frequently, which have a low-frequency modulating effect on TCs. The activity characteristics of TCs have changed significantly, and rare high-intensity TCs have frequently made landfall in China (Wu, 2023). The southeastern coastal area, as one of the most economically developed and densely populated regions in China, is the region most seriously affected by TCs. The southeastern coastal area, as one of the most economically developed and densely populated areas in China, is the area most seriously affected by TCs in China. Most TCs that affect China originate in the northwest Pacific Ocean, and their movement paths are influenced by the WPSH. Most TCs that affect China are generated in the northwest Pacific Ocean, and their movement paths are affected by the WPSH. Before TCs make landfall from the northwest Pacific Ocean, China's coastal urban agglomerations often experience regional multi-day severe O₃ pollution (Wang et al., 2022b). Although the frequency of TCs in the northwest Pacific Ocean has decreased in recent years, their average intensity has shown an upward trend (Yu et al., 2025; Jung, 2025; Wang et al., 2022a) and their duration has also become longer (Nayak and Takemi, 2023). Although the frequency of TCs in the northwest Pacific Ocean has decreased in recent years, their average intensity has shown an upward trend (Balaguru et al., 2024; Bhatia et al., 2022; Chand et al., 2022; Jung, 2025; Wang et al., 2022a), and their duration has also become longer (Kossin, 2018; Zhang et al., 2020). Yamaguchi and Maeda (2020) showed that although climate warming has accelerated the overall movement speed of TCs, their speed will slow down when they move toward the temperate zone during the poleward migration process, and the time they stay in a specific area will be extended. Affected by the surrounding atmospheric circulation, the slower the TCs move, the longer their impact duration and the greater their effects, which influence O₃ transport, extend the duration of O₃ pollution, exacerbate O₃ concentration, and expand the spatial extent of pollution. Global climate models (GCMs) are able to directly simulate surface O₃ concentrations under both historical and future scenarios (Turnock et al., 2020). These simulations provide an important reference for understanding the long-term evolution of surface O₃ driven by changes in emissions and climate. Affected by the surrounding atmospheric circulation, the slower the TCs move, the longer their impact time, and the greater the impact caused by the TCs, which will affect O₃ transmission, increase the duration of O₃ pollution, aggravate the degree of O₃ pollution, and expand the scope of pollution. In the context of global warming in the future, the increase in unfavorable meteorological conditions will make the O₃ pollution problem more serious (Fu and Tai, 2015; Keeble et al., 2017; Arnold et al., 2018; Akritidis et al., 2019; Saunier et al., 2020). Therefore, studying the trend of O₃ changes under future climate change scenarios is particularly important for formulating countermeasures against O₃ pollution.

The YRD is located in a key position in the eastern coastal economic zone of China. It is also a typical area frequently affected by TCs in the warm seasons (Wu et al., 2025; Qi et al., 2024). In addition, it has a high degree of urban agglomeration, dense population, and high energy consumption, making it a key area for air pollution prevention and controlmaking it a key prevention and control area for air pollution (Zhan et al., 2024; Bao et al., 2025). This study focuses on the regulatory mechanism of TCs on regional O₃ pollution and its impact on future pollution trends. First, based on the weather classification over the years, the characteristics of atmospheric circulation changes that cause O₃ changes are revealed, and the mechanism of the TC weather pattern in the YRD affecting O₃ pollution is clarified. Secondly, based on the data reconstruction method, the O₃ annual variation series is reconstructed according to the frequency and intensity of SWPs. Finally, based on future scenario data, the evolution characteristics of atmospheric circulation and the trend in O3 concentrations under different future scenarios are estimated, and the number of days when TC weather pattern appears and their contribution to O₃ variation are quantified. The research results help to fully and systematically understand the influence mechanism of weather conditions on O₃ pollution, provide a reference for the YRD to carry out targeted O₃ pollution control strategies, and have dual significance in improving regional air quality and advancing low-carbon development.

2 Materials and methods

2.1 O₃ observation data

The hourly pollutant monitoring data of 26 cities in the YRD used are derived from the National Environmental Monitoring Center of China. The platform provides pollutant concentration data updated every hour. To better describe the level of O₃ pollution at the urban scale, the arithmetic mean of the pollutant concentrations at each monitoring station was used as the pollutant concentration for of the city. O₃-8h represents the daily 8h average O₃ concentration data, which can more accurately characterize the long term exposure to regional O₃ pollution. Therefore, the O₃ data used in the analysis of this article all use the O₃-8h value, and the daily maximum 8-hour average concentration (unit: μg/m³) is taken as the daily O₃ concentration.— O₃-8h represents the daily maximum 8-hour average O₃ concentration, which can more accurately characterize the long-term exposure to regional O₃ pollution. The daily maximum 8-hour average O₃ concentration is calculated as the highest average O₃ mixing ratio over any consecutive 8-hour period within a calendar day (00:00–23:59 local time). Specifically, 8-hour moving averages are computed for all possible consecutive 8-hour windows (e.g., 00:00–07:59, 01:00–08:59, ..., 16:00–23:59), and the maximum value among them is recorded as the daily O₃ concentration. Therefore, the O₃ data used in the analysis of this article are all based on the O₃-8h value, and the daily maximum 8-hour average concentration (unit: μg/m³) is taken as the daily O₃ concentration.

2.2 Classification of synoptic weather patterns

Common objective weather classification methods mainly include principal component analysis, clustering algorithms, variance method based on correlation coefficients and neural network algorithms. We use orthogonal rotation principal component analysis in T mode (PTT) to classify SWPs in the YRD from 2018 to 2022. The PTT classification method has been integrated into the "cost733class" software. This method is an objective circulation classification method based on principal component analysis. By rotating the loadings of the T-mode principal components, its classification results are more physically interpretable (Philipp et al., 2016). It can accurately reflect the characteristics of the initial circulation field, does not change significantly due toacross different classification objects, and the obtained circulation spatio-temporal field is more stable (Huth et al., 2016). It has been widely used in research fields such as atmospheric circulation and air pollution (Hou et al., 2019; Gao et al., 2021).

The meteorological data are derived from the reanalysis data provided by the National Center for Environmental Prediction (NCEP). The dataset has a horizontal resolution of 2.5°×2.5°, with 144×73 grid points in the latitude-longitude domain and 17 vertical layers ranging from 1000 hPa to 10 hPa. Meteorological variables considered in this study include the 500 hPa geopotential height field, sea level pressure, 500 hPa wind field, 850 hPa wind field, 1000 hPa wind field, and vertical wind velocity. Considering that the geopotential height field at 850 hPa effectively minimizes the influence of surface conditions on atmospheric motion while capturing the variations of shallow meteorological systems (Shu et al., 2017). In this study, we used the geopotential height field at 850hPa from June to September during 2018–2022 to classify SWPs and analyze the three-dimensional structure of circulation fields associated with different SWPs. Considering that the 850 hPa geopotential height field effectively minimizes the influence of surface conditions on atmospheric motion while capturing the variations of shallow meteorological systems, this study utilizes the 850 hPa geopotential height field to classify SWPs and analyze the three dimensional structure of circulation fields associated with different SWPs.

2.3 Reconstruction of annual variation series of O₃ concentration

The change in SWPs includes the changes in SWP frequency and intensity. The change in SWP frequency refers to the number of occurrences of a certain type of SWP in different years, while the change in SWP intensity refers to the change in the average intensity of the weather system associated with a certain type of SWP across different years. To quantify the contribution of the change in SWP frequency and intensity to the annual change of O₃, Yarnal (1993) proposed a method to assess the influence of changes in SWP frequency on the annual change of O₃. The specific equation is as follows:

$$\overline{\overline{O_{3m}}}(fre) = \sum_{k=1}^{6} \overline{O_{3k}} F_{km}$$
 (1)

where $\overline{O_{3m}}(fre)$ represents the reconstructed mean O_3 concentration influenced by the frequency variation in SWPs for year m; $\overline{O_{3k}}$ represents the average O_3 concentration of a certain SWP in all years, and F_{km} represents the frequency of occurrence of SWP for year m.

Later, Hegarty et al. (2007) proposed that the impact of SWP changes on the annual variation of O₃ should take into account changes in both frequency and intensity. Therefore, Eq. (1) was modified as follows:

Page 5 of 37

$$\overline{\overline{O_{3m}}}(fre+int) = \sum_{k=1}^{6} (\overline{O_{3k}} + \Delta O_{3km}) F_{km}$$
 (2)

where $\overline{O_{3m}}(fre+int)$ represents the reconstructed mean O_3 concentration influenced by the frequency and intensity changes of SWPs for year m; ΔO_{3km} represents the modified anomaly concentration value obtained by fitting the SWP k intensity factor in the year m with the O_3 concentration anomaly value (ΔO_3) for that year, which represents the oscillation of the O_3 concentration value caused by the change in the intensity of the SWP k in year m. Hegarty et al. (2007) used the average sea level pressure value in the classification area to represent the SWP intensity change factor. Liu et al. (2019) used the same method to construct the annual O_3 variation series in North China, but used the lowest pressure value in the classification area as the SWP intensity factor.

Since the characteristic changes of each SWP that lead to the increase in O₃ concentration are different, when defining the SWP intensity factor, it is necessary to consider the unique change characteristics that lead to the increase in O₃ concentration for each SWP. To better describe the changes in SWP intensity, we selected the average, maximum, and minimum geopotential heights of different regions based on meteorological characteristics and the location of weather systems. The region with the largest correlation coefficient with the annual O₃ variation series was defined as the SWP intensity factor under that pattern. This part is explained in detail in Section 3.4.1. We select the SWP intensity factor in SWP1 as the maximum geopotential height in zone 7 (110°–130°E, 20°–35°N); SWP2 as the maximum geopotential height in zone 2 (90°–140°E, 20°–50°N); SWP3 as the minimum geopotential height in zone 4 (110°–130°E, 25°–40°N). We define the SWP intensity factor in SWP1 as the maximum geopotential height in zone 1 (115°–135°E, 20°–40°N); SWP2 as the maximum geopotential height in zone 2 (90°–140°E, 20°–50°N); SWP3 and SWP5 as the minimum geopotential height in zone 3 (110°–130°E, 10°–40°N); and SWP4 as the average geopotential height in zone 2 (90°–140°E, 20°–50°N).

2.4 CMIP6 future climate scenario data

Based on 18 models of the Sixth International Coupled Model Intercomparison Project (CMIP6) and the ERA5 dataset, a bias-corrected global dataset was constructed (Xu et al., 2021). The dataset covers the historical period from 1979 to 2014 and the future climate scenarios from 2015 to 2100, with a horizontal grid spacing of 1.25°×1.25° and a time interval of 6 hours. Considering that O₃ pollution often occurs under extreme weather conditions, the more extreme SSP5-8.5 scenario was selected for this study. This scenario is a high-forcing scenario, and the radiative forcing stabilizes at 8.5 W/m² by 2100. In addition, as China implements more and more energy-saving and emission reduction measures, especially with the establishment of carbon peak and carbon neutrality goals, future greenhouse gas emissions are expected to be effectively controlled. Therefore, the relatively mild SSP2-4.5 scenario was selected for comparison. This scenario is a moderate forcing scenario, and the radiative forcing stabilizes at 4.5 W/m² by 2100. We use the geopotential height field at 850 hPa from June to September during 2018 to 2022 (historical period), 2030 (carbon peak), 2035 (beautiful China), 2060 (carbon neutrality), and 2100 as the input for the PTT to classify weather patterns. We use the 850 hPa average potential height field from 2018 to 2022 (historical period), 2030 (carbon peak), 2030 (carbon peak), 2035 (beautiful China), 2060 (carbon neutrality), and 2100 to classify weather conditions.

3 Results and discussions

245

246

247

248

249

250

251

252

253

254

255

256

257258

259

260

261

262

263

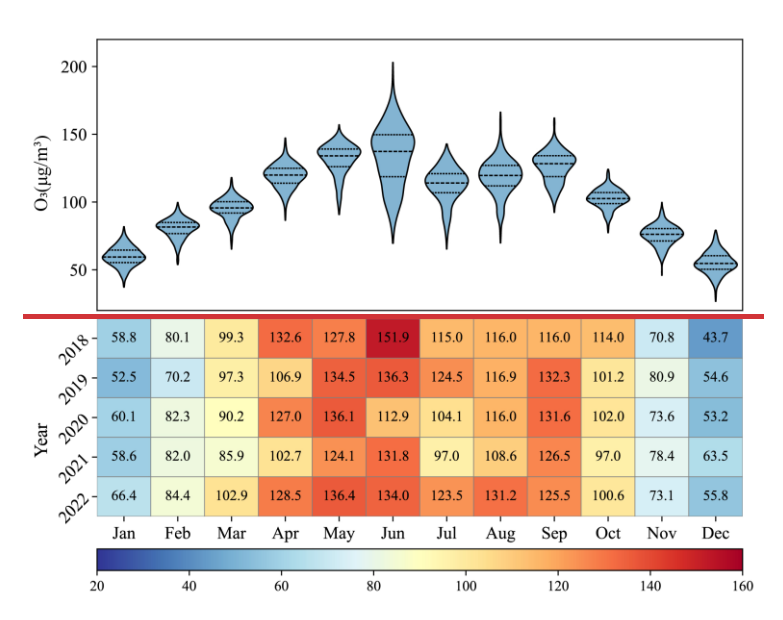
264

265

266267

3.1 Characteristics of O₃ pollution in the YRD

Figure 1 shows the monthly variation trend of ground-level O₃ concentrations and meteorological conditions (solar radiation, temperature, precipitation, and relative humidity) in the YRD from 2018 to 2022. It can be seen that the inter-month variations of O₃ concentrations present an M-shaped pattern. Figure 1 shows the monthly trends of ground level O₂ concentrations in the YRD from 2018 to 2022, inter month variations of O₃ concentrations present a M shaped pattern. From January to June, as the temperature rises and solar radiation increases, the O₃ concentration rises significantly and reaches the first peak (133.36 μg/m³). However, the increased precipitation and higher humidity in July exert a notable wet scavenging effect on O₃ precursors. O₃ concentration increases again and reaches the second peak (126.38 μg/m³) in September. From October to December, as the temperature gradually decreases and solar radiation weakens, the O₃ concentration shows a continuous downward trend, and reaches the lowest value of 54.17 µg/m³ of the year in December. The O₃ concentration shows obvious seasonal changes throughout the year. In summer, higher temperatures, stronger solar radiation, and longer sunshine duration jointly enhance atmospheric photochemical reactions, thereby significantly increasing the O₃ concentration. In winter, lower temperatures, weaker solar radiation, and shorter sunshine duration lead to a significant weakening of photochemical reactions, which is not conducive to the generation of O₃. From the kernel density curve, it can be seen that the distribution in summer months is wider, indicating that the O₃ concentration fluctuates greatly, while the distribution in winter months is narrower, indicating that the O₃ concentration changes are relatively stable in winter. This periodic variation reflects the high sensitivity of O₃ concentration in the YRD to meteorological conditions (temperature, solar radiation, humidity, wind speed, etc.), which affect the rate of photochemical reactions and thus affect the generation of O₃.



268

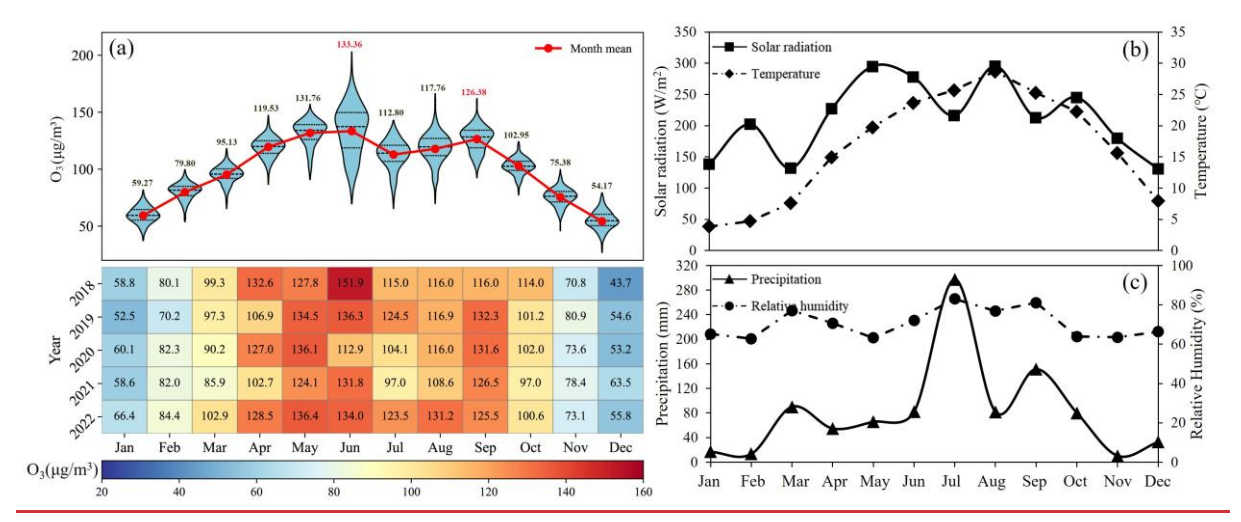


Figure 1. Inter-monthly variations in mean O₃ concentrations and associated meteorological conditions in the YRD from 2018 to 2022. (a) The monthly variation of O₃ concentrations is shown, with the red trend line representing the monthly mean values and the individual monthly concentrations labeled. (b-c) The variation trends of solar radiation, temperature, precipitation and relative humidity during the same period. (The shaded area in the violin plot represents the kernel density curve, with the three black lines indicating the 25th percentile, the mean, and the 75th percentile, respectively.) Inter-monthly variations of mean O₃-concentrations in the YRD from 2018 to 2022 (The region depicted in the violin plot corresponds to the kernel density curve, with the three black lines representing the 25th percentile, the mean, and the 75th percentile, respectively)

271

272

273

274

275

276

277

278

279

280

281

282

283284

285

286

287

288

289 290

291

292

293

294

295

296

297

298

299

300

301

O₃ pollution in the YRD is concentrated in warm months of the year. We analyzed the temporal distribution of O₃ concentrations in representative cities in the YRD (Shanghai, Nanjing, Hangzhou, and Hefei) from April to September during 2018-2022 (Fig. 2). Since TCs mainly occur after June, O₃ pollution is often associated with TC activity. During the same TC period, the O₃ concentrations in Shanghai, Nanjing, Hangzhou, and Hefei were different, but the temporal trends were similar. TCs have a certain impact on the changes in O₃ concentrations in the YRD. According to the evolution and trajectory of TC weather, TCs affecting China are primarily from the northwest Pacific Ocean (Zhan et al., 2020; Wang et al., 2024a). As they develop and move, these TCs will have a significant impact on O₃ concentrations in China (Xi et al., 2025). At this time, the YRD is located on the periphery of the TCs. Under the control of the periphery of the TCs, the strong downward airflow will make the YRD in stagnant weather conditions and inhibit the diffusion of pollutants (Shu et al., 2016), accompanied by high temperature, clear and dry weather conditions, which are the main weather conditions causing O₃ pollution. With the evolution of TC weather system, when the TCs center gradually approaches the YRD until it is within a certain range, the YRD is no longer under the influence of the periphery of the TCs and comes under the control of the TC wind and rain belt. Strong winds and precipitation can significantly cleanse air pollutants, and thereby reduce O₃ concentrations. After TCs dissipate, O₃ pollution levels may rise again due to restored meteorological conditions conducive to O₃ formation (Zhan et al., 2020). These results suggest that TCs can significantly affect O₃ pollution in the YRD, highlighting the importance of implementing O₃ control measures prior to TC landfall. O₃-pollution in the YRD is concentrated in warm months of the year. We analyzed the temporal distribution of O₂-concentrations in representative cities in the YRD (Shanghai, Nanjing, Hangzhou, and Hefei) from April to September during 2018 2022 (Fig. 2). Since TCs mainly occur after June, and O₃-pollution is often associated with TC activity. During the same TC period, the O₂ concentrations in Shanghai, Nanjing, Hangzhou, and Hefei were different, but the temporal trends were similar. However, the spatiotemporal characteristics of O₃ pollution vary during

303

304

305

306

307

308

309

310311

312

313

314

315

316

317

318

319

320 321

322

323

different TCs and can be divided into two main trends: the O3 concentration first increases and then decreases, or first increases, then decreases and then increases. The similarity is that when the TCs are generated, the O₃ concentrations in typical cities in the YRD are higher than the previous day. According evolution and trajectory of TC weather, TCs affecting China are primarily generated in the northwest Pacific Ocean. At this time, the YRD is located on the periphery of the TCs. Under the control of the periphery of the TCs, the strong downward airflow will make the YRD in stagnant weather conditions and inhibit the diffusion of pollutants (Shu et al., 2016), accompanied by high temperature, clear and dry weather conditions, which are the main weather conditions causing O3 pollution. With the the YRD is no longer under the influence of the periphery of the TCs and comes under the is often accompanied by strong winds and precipitation, significantly cleanse atmospheric pollutants, thereby reducing the O₃ concentration. Therefore, when the TCs gradually approach the YRD from the formation to the dissipation of the TCs, the YRD will change from being controlled by the periphery of the TCs to being controlled by the low pressure center, thus forming a trend of O₃ concentration first increasing and then decreasing. After the TCs dissipate, O₃ levels may rise again due to restored meteorological conditions conducive to O₃ formation (Zhan et al., 2020). It can be seen that TCs may have an impact on the O₃ pollution in the YRD to a certain extent, highlighting the importance of implementing O₃-pollution control measures before TCs landfall.

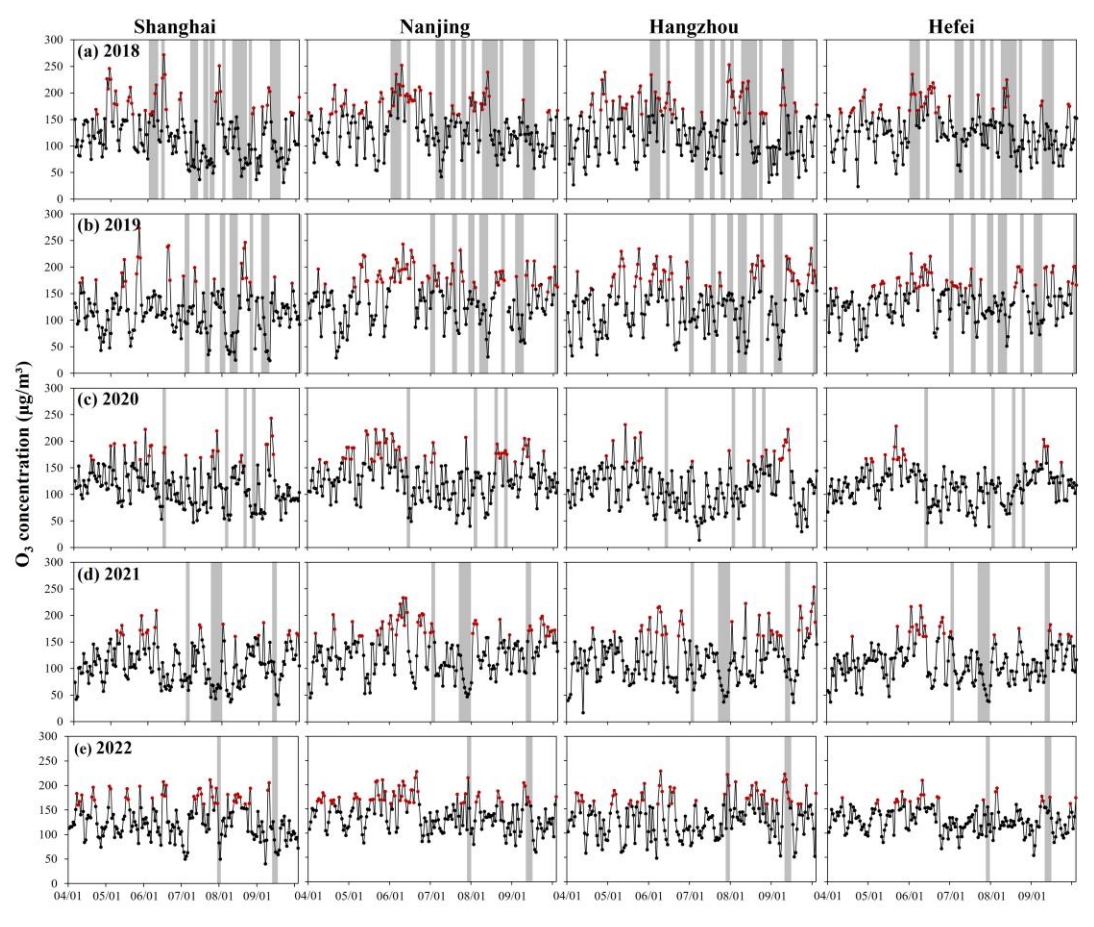


Figure 2. Changes in O₃ concentration in Shanghai, Nanjing, Hangzhou, and Hefei from April to September in 2018 to 2022. The gray shadows mark the time of impact of the TCs weather that landed, and the red dots are O₃-polluted days.

3.2 Main synoptic weather patterns in the YRD

324

325 Based on the analysis of O₃ variation characteristics in the YRD, O₃ concentrations were generally high from June to September, coinciding with the peak season of TC activity. We selected June to 326 327 September during 2018-2022 as the research period and used the PTT weather classification method to 328 classify the weather situation. SWPs in the YRD during this period were primarily divided into four 329 categories. As shown in Table 1, SWP1 is the main SWP, occurring on 383 days and accounting for 330 62.79 % of the period. SWP2 and SWP4 followed, occurring on 81 and 80 days, respectively, with 331 frequencies of 13.28 % and 13.11 %. SWP3 was less frequent, occurring on 10.82 % of days. Specifically, 332 SWP1 was mainly influenced by the southwesterly flow introduced by the WPSH and the northeast China 333 low, SWP2 by northwesterly flow introduced by a continental high and the northeast China low, SWP3 334 by southeasterly flow introduced by the WPSH, and SWP4 by northeasterly flow introduced by the 335 WPSH and TCs. 336 Statistics of average O₃ concentrations and meteorological factors under each SWP indicate that SWP4 337 had the lowest average O₃ concentration (115.07 μg/m³), whereas SWP2 had the highest value (132.36 μg/m³). O₃ concentrations during SWP1 and SWP3 were similar, at 123.81 μg/m³ and 123.28 μg/m³, 338 339 respectively. However, significant differences in O₃ concentrations were observed among SWPs during 340 the same period, highlighting the strong influence of circulation patterns on O₃ pollution levels. SWP1 341 exhibited higher temperatures (27.12 °C), favoring increased O₃ concentrations. SWP2 was influenced by dry northwesterly airflow, exhibiting lower humidity (76.74 %) and slower wind speed (2.03 m/s), 342 343 which hindered air pollutant dispersion and resulted in higher O₃ concentrations. SWP3 was 344 characterized by lower humidity (78.53 %) and slower wind speed (2.11 m/s), which were key factors 345 contributing to increased O₃ concentration. Under SWP4, though TCs far from the coastline could lead 346 to regional O₃ pollution (in section 3.3.2), the landfalling TCs could bring strong winds and rainstorms, 347 increasing humidity (80.03 %) and wind speed (2.64 m/s), which resulted in lower average O₃ 348 concentrations. 349 To further explore the relationship between atmospheric circulation and O₃, the rotated orthogonal 350 principal component analysis method was used to classify the weather in the YRD. The first dominant 351 five SWPs were selected, and the remaining SWPs were defined as unclassified. A total of 1801 days 352 were classified, and the remaining 25 days were unclassified weather patterns. As shown in Table 1, 353 SWP1 and SWP2 are the main SWPs, with 980 and 570 days of occurrence, respectively, accounting for 354 53.67% and 31.22%. The occurrence frequencies of SWP3, SWP4, SWP5, and UP SWPs were lower, at 355 5.15%, 4.93%, 3.67%, and 1.37%, respectively. Table 1 also shows the seasonal occurrence frequencies 356 of the five SWPs, and the seasonal occurrence frequencies of each SWP differ significantly. SWP1 has 357 the highest occurrence frequency in winter, at 44.39%, followed by spring (29.49%), autumn (24.80%), 358 and summer (1.33%). SWP2 mainly occurs in summer, with the highest frequency in summer, reaching 66.49%, followed by spring (25.09%). SWP3 and SWP4 appear most frequently in autumn, at 79.79% 359 and 68.89% respectively. SWP5 appears most frequently in summer (61.19%), followed by autumn 360 361 (32.48%). 362 Statistics of O2-concentration and meteorological factors under each SWP show that the average O2 363 concentration for SWP1 is relatively low (87.60 µg/m²), and the O₃ concentration under SWP2 reaches 364 the highest (121.49 µg/m³). The O₃-concentrations under SWP3, SWP4, and SWP5 are similar, which are 107.89 μg/m³, 106.66 μg/m³, and 109.50 μg/m³ respectively. The difference in O₃ concentration under 365 different SWPs is not only related to the seasonal frequency of occurrence but also closely related to the 366

specific circulation field situation. For example, SWP2 and SWP5 with high O₃-concentrations are both SWPs with a higher frequency of occurrence in summer, but there are significant differences in O₃ concentrations between SWP2 and SWP5, which reflects the important influence of the circulation pattern on O₃-concentration. Specifically, SWP1 is mainly controlled by the northwest wind guided by the continental high pressure and the northeastern low pressure, SWP2 is mainly controlled by the southwest wind guided by the WPSH and the southwest vortex, SWP3 is mainly controlled by the southeast wind guided by the WPSH, SWP4 is mainly controlled by a saddle shaped pressure field, mainly with northerly winds, and SWP5 is mainly controlled by the northeasterly winds influenced by the WPSH and TCs.

Table 1. The occurrence days and frequencies of various SWPs in the YRD from 2018 to 2022, the frequency of occurrence of each SWP across the four seasons, average O₃ concentrations and meteorological factors and the meteorological factors associated with each SWP.

| <u>Type</u> | Number of days (frequency) | O ₃ concentration _(μg/m ³)_ | Temperature (°C) | Relative humidity (%) | Wind speed (m/s) |
|-------------|----------------------------|--|------------------|-----------------------|------------------|
| SWP1 | 383(62.79%) | 123.81 | <u>27.12</u> | 80.80 | 2.19 |
| SWP2 | 81(13.28%) | <u>132.36</u> | <u>25.00</u> | <u>76.74</u> | <u>2.03</u> |
| SWP3 | 66(10.82%) | 123.28 | <u>25.68</u> | <u>78.53</u> | <u>2.11</u> |
| SWP4 | 80(13.11%) | <u>115.07</u> | <u>26.61</u> | 80.03 | <u>2.64</u> |

Notes: "*" Indicates weather conditions that were not classified and no statistical analysis was performed. Figure 3 illustrates the three-dimensional atmospheric circulation structures of SWP1, SWP2, and SWP3. For SWP1, at 850 hPa, the YRD was located northwest of the WPSH and south of the northeast China low. This influence was controlled by southwesterly flow, which was jointly guided by the WPSH and the northeast China low (Fig. 3a). Warmer southerly winds promoted temperature increases in the YRD, and elevated temperatures enhanced photochemical reactions producing O₃. At sea level, the WPSH shifted northeastward, influencing the YRD through southerly flow (Fig. 3d). These southerly winds transported pollutants from the PRD to the YRD. The combined effects of enhanced photochemical reactions and interregional advection contributed to elevated O₃ concentrations in the YRD under SWP1. At 500 hPa, the YRD was dominated by straight westerly flows (Fig. 3g), indicating intensified subsidence.

For SWP2, the YRD was located east of the continental high and southwest of the northeast China low. This influence was driven by northwesterly flow, which was jointly guided by the continental high and the northeast China low (at 850 hPa, Fig. 3b). These dry northwesterly winds significantly reduced relative humidity in the region. At sea level, the YRD was primarily controlled by the continental high (Fig. 3e). At 500 hPa, downward airflow strengthened over the northern YRD behind the trough (Fig. 3h). The significantly lower relative humidity and slower wind speeds favored the formation and accumulation of O₃, ultimately leading to increased O₃ concentrations under this pattern.

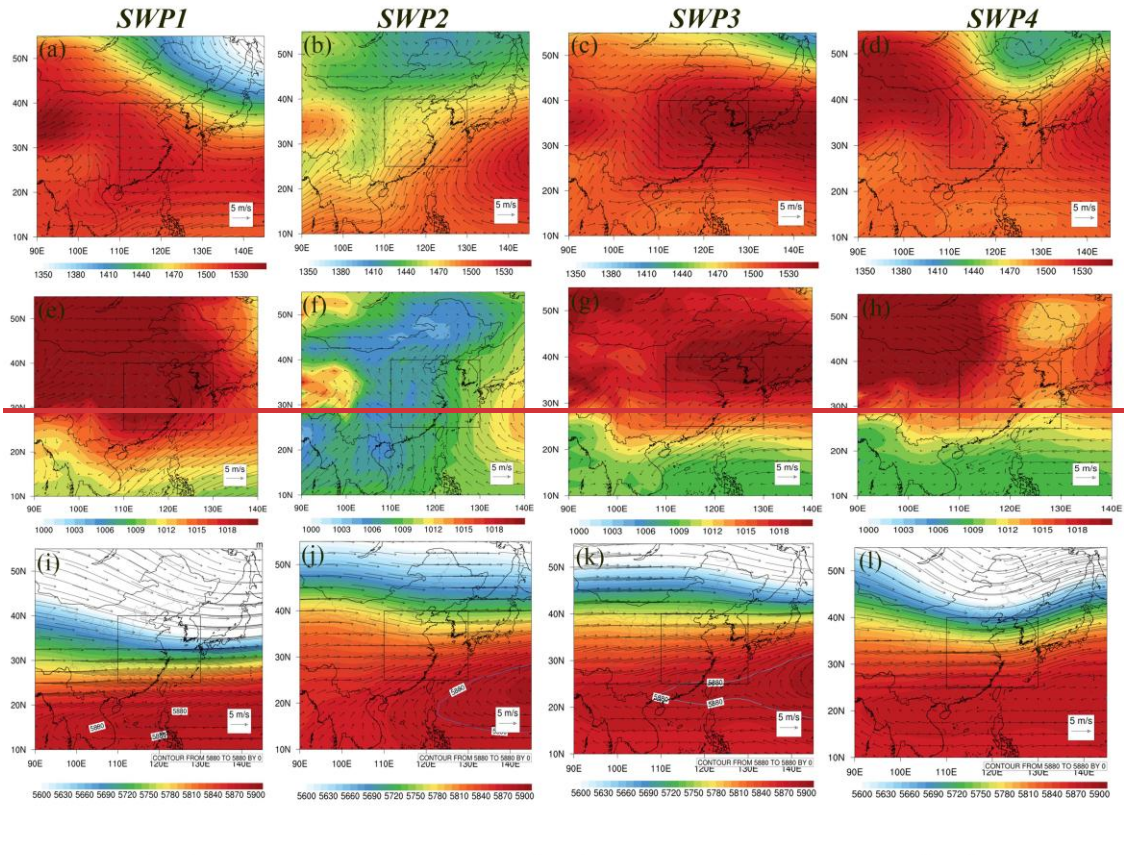
For SWP3, at 850 hPa, the YRD was located southwest of the WPSH and was controlled by southeasterly flow at its southern edge (Fig. 3c). This southeasterly airflow from the ocean increased regional humidity and lowered temperatures. At sea level, the WPSH shifted northward, and the YRD was affected by easterly winds controlled by a tropical depression (Fig. 3f). At 500 hPa, the YRD was

 located near the edge of the WPSH or close to a low-pressure trough (Fig. 3i). As the WPSH weakened and retreated eastward, its intensity and position suppressed convective activity, leading to a dominant downdraft. This downdraft, combined with lower horizontal wind speeds, hindered the diffusion of pollutants, resulting in increased O₃ concentrations. Figure 3 shows the three dimensional atmospheric circulation structure of SWP1, SWP2, SWP3, and SWP4. For SWP1, the YRD is located east of the continental high pressure and southwest of the northeastern low pressure, and is affected by the northwest wind influenced by both the continental high pressure and the northeastern low pressure (at 850 hPa as shown in Fig. 3a). At sea level, the YRD is mainly controlled by the continental high pressure (Fig. 3e). At 500 hPa, the YRD is controlled by westerly winds (Fig. 3i). The adverse effects of low temperature and weak solar radiation in winter on O₃ photochemical reactions are the main reasons for the low O₃ concentration under SWP1.

For SWP2, the YRD is located to the northwest of the WPSH, and the southeast side is also affected by the southwest low vortex (Fig. 3j). At 850 hPa, the YRD is controlled by the southwest wind influenced by the WPSH and the southwest vortex (Fig. 3b). The warmer southerly winds are conducive to the increase in temperature in the YRD, and high temperature is conducive to the photochemical reaction to produce O₃. At sea level, the WPSH shifts to the northeast, and the YRD is affected by the southerly wind (Fig. 3f). The southerly wind will transport pollutants from the PRD to the YRD. The combined effect of enhanced photochemical reactions and inter regional advection transport causes the YRD to have a higher O₃ concentration under SWP2.

For SWP3, at 850 hPa, the YRD is located to the southwest of the WPSH and is controlled by the southeasterly winds at its southern edge (Fig. 3c). At sea level, the WPSH shifts northward, and the YRD is affected by northeasterly winds influenced by the tropical depression (Fig. 3g). At 500 hPa, the YRD is located at the edge of the WPSH or near the low pressure trough (Fig. 3k). The intensity and position of the WPSH suppresses convective activity, resulting in the dominance of sinking airflow. Under SWP3, the YRD is controlled by southeasterly airflow from the ocean, which increases the regional humidity. As an autumn SWP, the average temperature of SWP3 is relatively low, and the meteorological conditions are generally not conducive to the generation of O₃ by photochemical reactions.

For SWP4, at 850 hPa, the YRD is mainly controlled by a saddle shaped pressure field, located between two high pressure systems and two low pressure systems, and the wind speed in the YRD is relatively small (Fig. 3d). At sea level, the situation is similar (Fig. 3h). At 500 hPa, the YRD is located behind a weak trough (Fig. 3l), resulting in a weak subsidence near the surface. Under this weather situation, the YRD is mainly stagnant weather, and the subsidence and low horizontal wind speeds hinder the diffusion of pollutants, resulting in O₃ pollution.



434 435

436

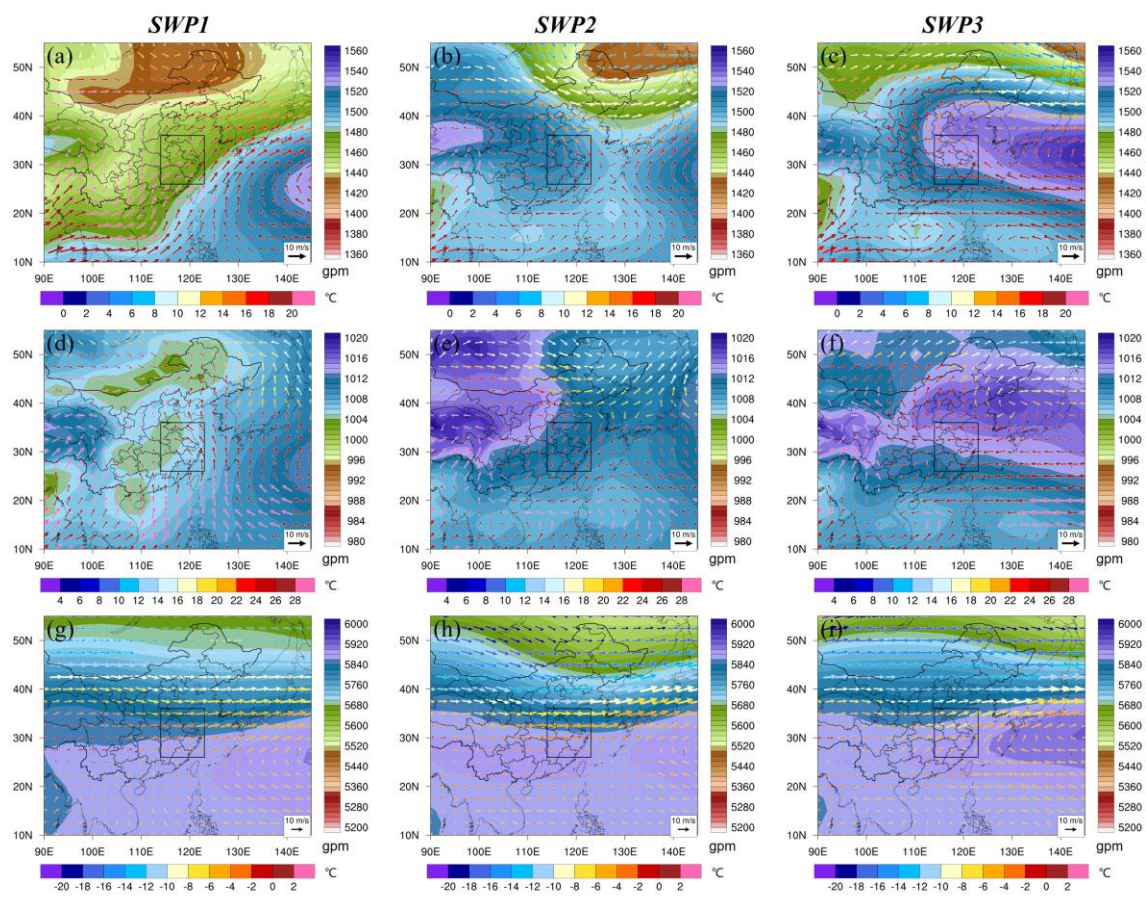


Figure 3. The average weather conditions in SWP1, SWP2 and SWP3, including an 850 hPa geopotential height field superimposed on wind field (a-c), sea level pressure field superimposed on 1000 hPa wind field (d-f), a 500

hPa geopotential height field superimposed on wind field (g-i). In (a)-(i), shading represents geopotential height and color vectors represent wind with temperature. The black frame in (a)-(i) includes the YRD. The average weather conditions in SWP1, SWP2, SWP3 and SWP4, including an 850 hPa geopotential height field superimposed on wind field (a d), sea level pressure field superimposed on 1000 hPa wind field (e h), a 500 hPa geopotential height field superimposed on wind field (i-l). In (a)-(l), shading represents geopotential height and black vectors represent wind. The black frame in (a)-(i) includes the YRD.

3.3 The important role of TCs on regional O₃ pollution

443

444

445

446

447

448

449

450

451

452

453

454

455

456

457

458 459

460

461

462

463

464

465

466

467

3.3.1 The impact of TC weather pattern (SWP5SWP4) on O3 pollution in the YRD

Figure 4 illustrates the three-dimensional atmospheric circulation structure under the TC weather pattern (SWP4). For the TC weather pattern, similar circulation conditions were observed at 850 hPa (Fig. 4a) and at sea level (Fig. 4b). The YRD was located northwest of the TCs and was controlled by northeasterly flow guided by the TCs. The direction and intensity of the northeast wind had a significant impact on meteorological conditions and pollutant transport in the YRD. At 500 hPa, the region was dominated by westerly or northwesterly flow (Fig. 4c). Meanwhile, the peripheral downward airflow associated with lower-level TCs (Fig. 4d) led to a more stagnant atmosphere over the YRD. As the TC approaches the YRD, strong northeasterly flow increased clean sea airflow transportation to the region, lowered temperatures and increased humidity, creating unfavorable meteorological conditions for photochemical reactions. Furthermore, higher wind speeds facilitated air pollutant elimination, leading to a decrease in O₃ concentrations in the region (Table 1). Figure 4 shows the three dimensional atmospheric circulation structure under the TC weather pattern (SWP5). For SWP5, similar circulation conditions are shown at 850 hPa (Fig. 4a) and sea level (Fig. 4b). The YRD is located to the northwest of TCs and is controlled by northeasterly winds guided by the TCs. The direction and intensity of the northeast wind have an important impact on the meteorological conditions and pollutant transport in the YRD. At 500 hPa, it is controlled by northerly or northwesterly flow (Fig. 4c). As SWP5 is a highfrequency pattern in summer, the meteorological factors of high temperature, low humidity, and strong solar radiation provide a favorable environment for photochemical reactions, thereby promoting the formation of O2. At the same time, under the influence of lower level TCs, the YRD is controlled by sinking airflow (Fig. 4d). The periphery downward airflows of the TCs make the atmosphere over YRD more stagnant, which cause the air hotter, dryer and more intense radiation (Table 1). This kind of weather pattern hinders the diffusion of pollutants, is easier for pollutants to accumulate in local areas, and thereby is conducive to the formation of O₃ accumulation.

Page 14 of 37

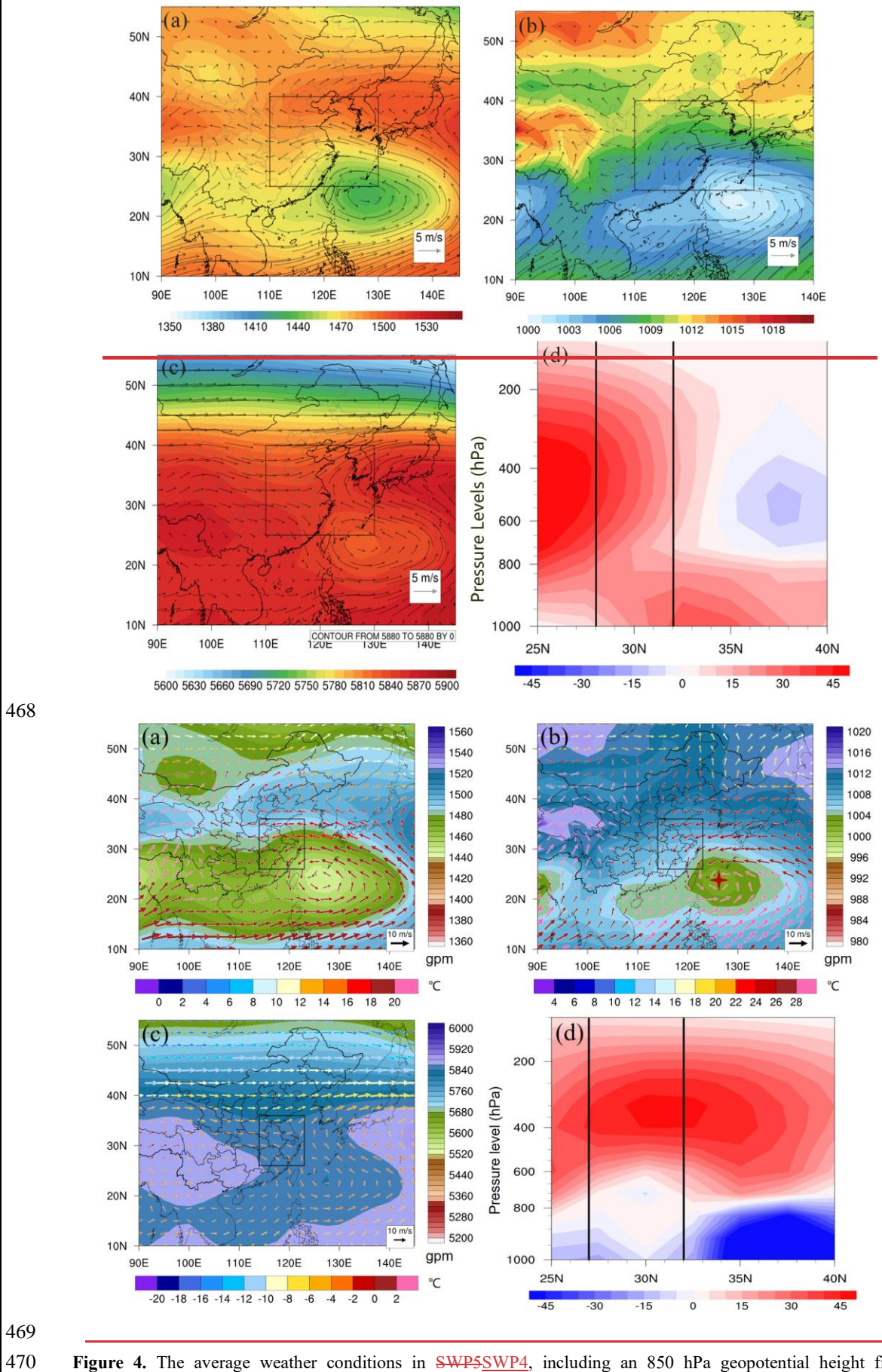


Figure 4. The average weather conditions in SWP5SWP4, including an 850 hPa geopotential height field

- superimposed on wind field (a), sea level pressure field superimposed on 1000 hPa wind field (b), a 500 hPa geopotential height field superimposed on wind field (c), height-latitude cross-sections of vertical velocity (unit: 10⁻² Pa·s⁻¹) between 25°N and 40°N (d). In (a)-(c), shading represents geopotential height and color vectors represent wind with temperature shading represents geopotential height and black vectors represent wind. The black frame in (a)-(c) and the vertical line area in (d) includes the YRD.
 - 3.3.2 Changes of atmospheric circulation field with different O₃ pollution levels under TC weather pattern

476

477

478 To better explore the relationship between O₃ pollution and the TC weather pattern (SWP4), O₃ 479 pollution was further classified into clean type (C), local pollution type (LP), and regional pollution type 480 (RP) based on pollution characteristics. RP was defined as all days when more than 20 % (> 5) of the 26 481 cities in the YRD recorded a maximum daily O₃ concentration exceeding 160 µg/m³, LP was defined as 482 all days when fewer than 20 % (< 5) of the 26 cities in the YRD recorded a maximum daily O₃ 483 concentration exceeding 160 µg/m³, and C included the remaining days not classified as LP or RP. Table 484 2 presents the number of days and frequencies of C, LP, and RP under SWP4. The frequencies of 485 SWP4 C, SWP4 LP, and SWP4 RP were 56.25 %, 18.75 %, and 25.00 %, respectively. The average O₃ 486 concentrations under these three types were 93.46 µg/m³, 126.97 µg/m³, and 161.19 µg/m³. The clean 487 type occurred more than half the time, contributing to the lower average O₃ concentration (115.07μg/m³) 488 under SWP4 (Table 1). Under the TC weather pattern, meteorological factors corresponding to different 489 O₃ pollution characteristics varied significantly (Table 2). As pollution levels increased, regional air 490 temperatures gradually rose, relative humidity decreased, and surface wind speeds decreased 491 significantly. These high temperatures, low humidity, and low wind speeds created favorable conditions 492 for O₃ formation and accumulation. Higher temperatures accelerated photochemical reactions, thereby 493 promoting O₃ production. Low humidity reduced the inhibitory effect of water vapor on photochemical 494 reaction chains, favoring further O₃ accumulation. Reduced wind speeds led to poor atmospheric 495 diffusion, hindering the dilution and transport of precursors and O₃. Overall, as pollution levels increased, meteorological conditions under the TC weather pattern gradually became more favorable for O₃ 496 497 formation and accumulation. To better explore the relationship between O₃ pollution and TC weather 498 pattern (SWP5), O₃ pollution is further divided into clean type (C), local pollution type (LP), and regional 499 pollution type (RP) according to the pollution characteristics. RP is defined as all days when more than 500 20% (> 5) of the 26 cities in the YRD have a maximum daily O₃-concentration of more than 160 μg/m³, LP is defined as all days when fewer than 20% (< 5) of the 26 cities in the YRD have a maximum daily 501 502 O₃ concentration of more than 160 µg/m³, and C is defined as the remaining days excluding LP and RP. 503 Table 2 shows the number of days and frequencies of C, LP, and RP under SWP5. Among them, the 504 frequencies of SWP5 C, SWP5 LP, and SWP5 RP are 55.22%, 17.91%, and 26.87% respectively. The 505 seasonal distribution characteristics of different degrees of O₃ pollution types in the TC weather pattern 506 are further discussed. Under SWP5, the number of days of local pollution and regional pollution in the 507 YRD is concentrated in summer and autumn. Local pollution is more likely to occur in autumn, with a 508 frequency of 58.33%, and regional pollution is more likely to occur in summer, with a frequency of 509 72.22%.

- Table 2. The number of days and frequency of occurrence of clean type (C), <u>local pollution type-lightly polluted type</u>
 (LP), and <u>regional pollution type-heavily polluted type</u> (HPRP) under each SWP, <u>average O₃ concentrations and</u>
- 512 meteorological factors associated with each type, the frequencies of their occurrence in four seasons.

| <u>Type</u> | | Number of days (frequency) | O ₃ concentration (µg/m³) | Temperature (°C) | Relative humidity (%) | Wind speed (m/s) |
|-------------|---------|----------------------------|--------------------------------------|------------------|-----------------------|------------------|
| | SWP4_C | 45(56.25%) | 93.46 | <u>25.57</u> | 82.06 | 2.98 |
| SWP4 | SWP4_LP | 15(18.75%) | 126.97 | <u>27.14</u> | <u>79.28</u> | <u>2.65</u> |
| | SWP4_RP | 20(25.00%) | <u>161.19</u> | <u>28.54</u> | 76.03 | 1.87 |

Figure 5 shows the structural characteristics of the three dimensional atmospheric circulation field with different O₃ pollution levels (SWP5 C, SWP5 LP, and SWP5 RP) under the SWP5. It illustrates that, for SWP5 C (Fig. 5a, d and g), the TCs are close to the YRD (Fig. 5d), and then bring strong winds and rainstorms to the YRD, which is not conducive to the accumulation of air pollutants and the generation of O₂ by photochemical reactions. At the same time, the high wind speed and rainfall scouring are conducive to the removal of pollutants. Therefore, clean days occur in the YRD under the influence of the TCs. For SWP5 LP (Fig. 5b, e and h), the TCs are located to the east of and a little far away from the YRD (Fig. 5). For the SWP5 RP (Fig. 5c, f and i), the center of TCs are located in the area around (25°N, 135°E). At 850 hPa (Fig. 5a, b and c), the changes of TCs are similar to those at 1000 hPa (Fig. 5d, e and f). At 500 hPa, a weak ridge appears as the pollution level deepens (Fig. 5g, h and i). The prevailing sinking airflow under the control of the WPSH can be strengthened by the TC activity, making the atmosphere more stagnant, and the meteorological conditions of high temperature and low humidity appear, causing the outbreak of O₃-pollution in the YRD (Shu et al., 2016). Among them, when local O₃ pollution occurs in the YRD, the TCs are slightly farther from the YRD, and their peripheral influence reaches the coastal areas (Fig. 5e). When regional O₃ pollution occurs in the YRD, the TCs are closer to the YRD, and their peripheral sinking effect is stronger over the YRD (Fig. 5f). In summary, when the TCs are located at 130°-135°E and 20°-30°N, the YRD is affected by the sinking airflow of the TCs, and high-concentration O₃-pollution is easily formed.

Figure 5 illustrates the structural characteristics of the three-dimensional atmospheric circulation fields corresponding to different O₃ pollution levels (SWP4_C, SWP4_LP, and SWP4_RP) under SWP4. For SWP4_C, at 850 hPa, the YRD was controlled by the TCs (Fig. 5a). The TCs brought strong winds and rainstorms to the YRD, which were not conducive to the accumulation of air pollutants or to O₃ formation via photochemical reactions. Simultaneously, high wind speeds and rainfall facilitated pollutant removal. When the TCs made landfall in the YRD (Fig. 5d), significant updrafts occurred in the lower atmosphere, favoring pollutant dispersion. Consequently, clean days were observed in the YRD under the influence of TCs. For the local and regional pollution patterns (SWP4_LP and SWP4_RP), TCs were generally 500–1000 km from the YRD coastline (Fig. 5e and f). Previous studies have shown that downdrafts caused by the outer airflow of TCs before landfall led to more stable atmospheric conditions (Zhan et al., 2020; Zhan and Xie, 2022). Under SWP4_LP and SWP4_RP, the YRD experienced higher temperatures and lower humidity (Table 2). These meteorological conditions favored O₃ formation, leading to the occurrence of O₃ pollution events.

For SWP4_LP, the warm high pressure over North China weakened, and the TC shifted westward, closer to the coastline (Fig. 5e). At 850 hPa, pollutant air masses from the PRD were transported to the YRD, but were diluted by clean air from the ocean (Fig. 5b). Compared to SWP4_RP, SWP4_LP had stronger winds and higher relative humidity (Table 2). Consequently, O₃ pollution in the YRD was slightly lower under SWP4_LP than under SWP4_RP. For SWP4_RP, the warm high pressure over North China weakened further, and the TC shifted eastward compared to SWP4_LP (Fig. 5c). The YRD was

dominated by strong downdrafts induced by the peripheral flows of the TC (Fig. 5f). This downdraft reinforced stagnant weather, suppressed convective activity, and hindered pollutant dispersion (Shu et al., 2016; Xi et al., 2025). Combined with meteorological analysis in Table 2, the temperature in the YRD under SWP4_RP was higher (28.54 °C), the relative humidity was lower (76.03 %), and the wind speed was slower (1.87 m/s), all of which favored photochemical reactions and limited pollutant dispersion. Furthermore, downdrafts induced by the peripheral flows of the TC promoted pollutant accumulation, significantly increasing the frequency of O₃ pollution. In summary, when the TC was located at 130°–135°E and 20°–30°N, the YRD was influenced by its sinking airflow, facilitating the formation of O₃ pollution.

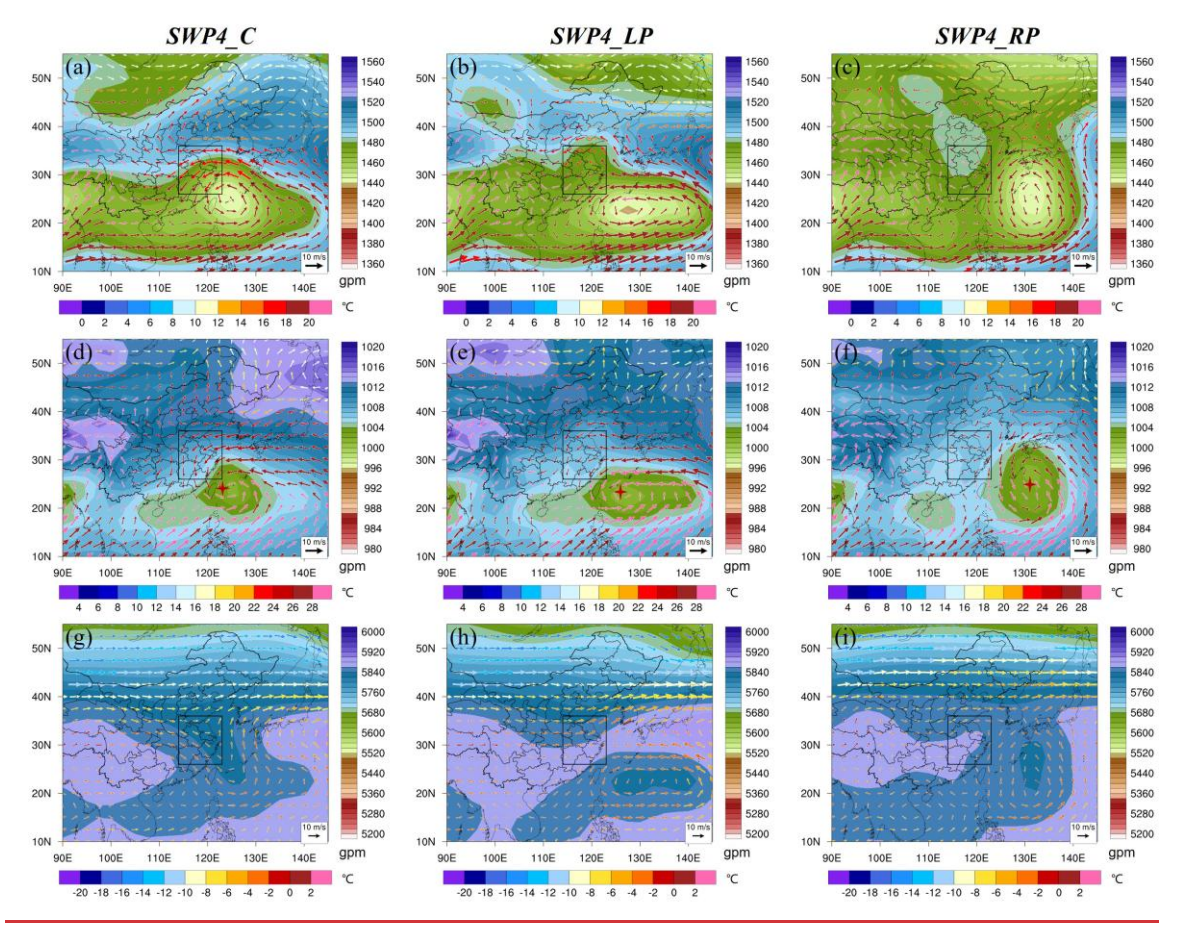


Figure 5. The average weather conditions in SWP4_C (left), SWP4_LP (middle), and SWP4_RP (right), including an 850 hPa geopotential height field superimposed on wind field (a-c), sea level pressure field superimposed on 1000 hPa wind field (d-f), a 500 hPa geopotential height field superimposed on wind field (g-i). The shading represents geopotential height, black vectors represent wind and the black frame includes the YRD, and the red asterisk in (d-f) indicates the location where the TCs made landfall.

3.4 To what extent TCs impact regional O₃ pollution in the YRD

3.4.1 The role of changes in the intensity and frequency of SWPs in the reconstruction of the annual variation series of O_3

<u>Different dominant SWPs produced varying near-surface meteorological conditions, which in turn</u> affected atmospheric processes such as O₃ photochemical production, transport, diffusion, and wet and

570

571

572

573

574

575

576

577

578

579

580

581

582

583

584

585 586

587

588 589

590

591

592

593

594

595

596 597

598

599

600

601

602

603

604

605

606

dry deposition. Changes in the frequency and intensity of SWPs were two key factors influencing O₃ concentration variations. We reconstructed the annual time series of O₃ concentrations from June to September between 2018 and 2022 by considering only changes in SWP frequency (fre) and changes in both SWP intensity and frequency (fre+int). In our study, we first removed the influence of emission sources on O₃ concentrations based on the results of Yan et al. (2024). Subsequent analyses were conducted using O₃ concentration series that were free from emission source influences. Using the O₃ trend reconstruction method, we quantified the contribution of SWPs to annual variations in O₃ concentrations from June to September.

Figure 6 illustrates the annual variations of reconstruction O₃ concentrations from June to September during 2018 to 2022. When only changes in SWP frequency were considered, the reconstructed time series was relatively flat and did not adequately capture the variation trend of O₃ concentrations. Therefore, changes in SWP frequency had minimal impact on the annual variation of O₃. When changes in SWP intensity were considered, the reconstructed series more closely resembled the original annual variation series. Therefore, compared to changes in SWP frequency, changes in SWP intensity contributed more to variations in O₃ concentration. To accurately assess the impact of both SWP frequency and intensity on annual O3 variation, we quantitatively calculated their contributions. The contribution index was defined as the ratio of the interannual variation amplitude of the reconstructed series to that of the original series, i.e., (O_{3max} of the reconstructed series - O_{3min} of the reconstructed series) / (O_{3max} of the original series – O_{3min} of the original series). When only changes in SWP frequency were considered, their contribution to the interannual variation was 10.05%. When changes in SWP intensity were additionally included, the contribution increased to 69.66%. This indicates that, compared with changes in SWP frequency, changes in SWP intensity played a more important role in driving interannual variations in O₃ concentrations. Figure 6 shows the annual variations of O₃ reconstruction concentrations from 2018 to 2022. It can be seen that when only the change in SWP frequency is considered, the reconstructed time series is relatively flat and cannot well show the downward trend of O₃ concentrations from 2019 to 2021. So, the change in SWP frequency has minimal impact on the annual variation of O₃. When the change in SWP intensity is considered, the reconstructed curve is closer to the original annual variation curve. Therefore, compared to the change in SWP frequency, the change in SWP intensity contributes more to the change in O₃ concentration. To accurately evaluate the impact of both SWP frequency and intensity on the annual variation of O₃ concentration, we quantitatively calculated the contribution of SWP frequency and intensity. The contribution index is defined as the ratio of the range (difference between the maximum and minimum values) of the reconstructed sequence to the range of the original sequence. When only the change in SWP frequency is considered, since the O3 concentration value in 2020 is lower than that in 2021 in the reconstructed data, its reduction contribution rate is 0%, while when the change in SWP intensity is added, the reduction contribution rate is 81.39%. It can be seen that compared to the change in SWP frequency, the change in SWP intensity is a more significant factor contributing to the change in O₂-concentration.

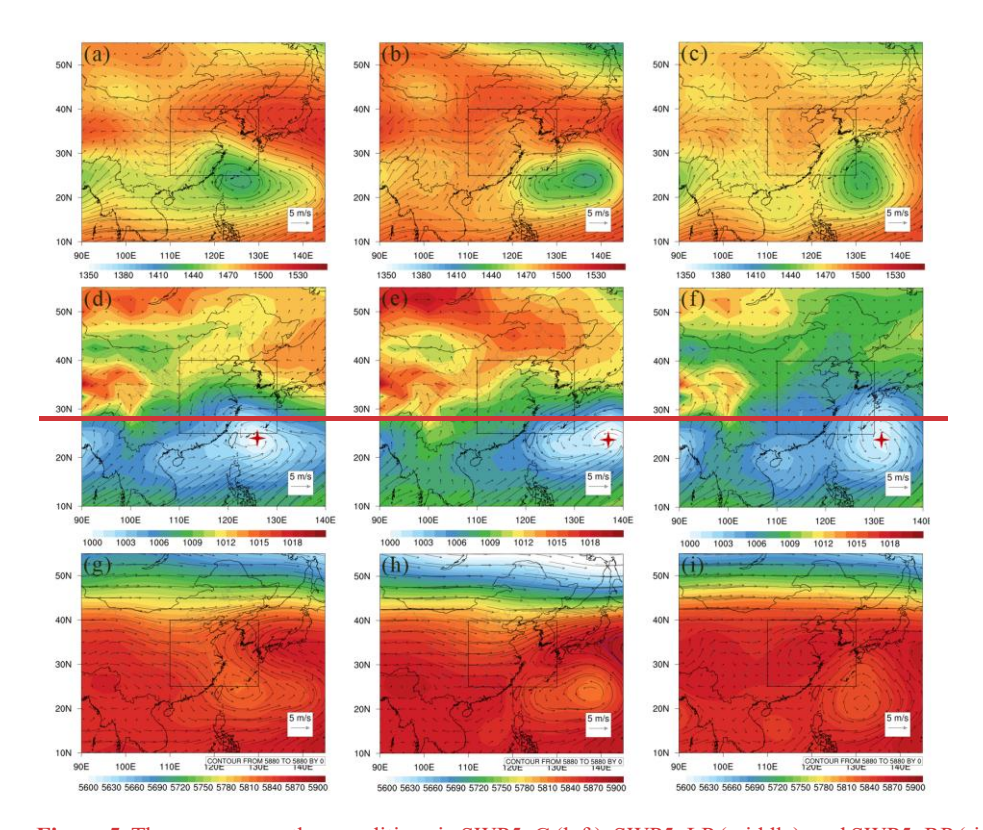
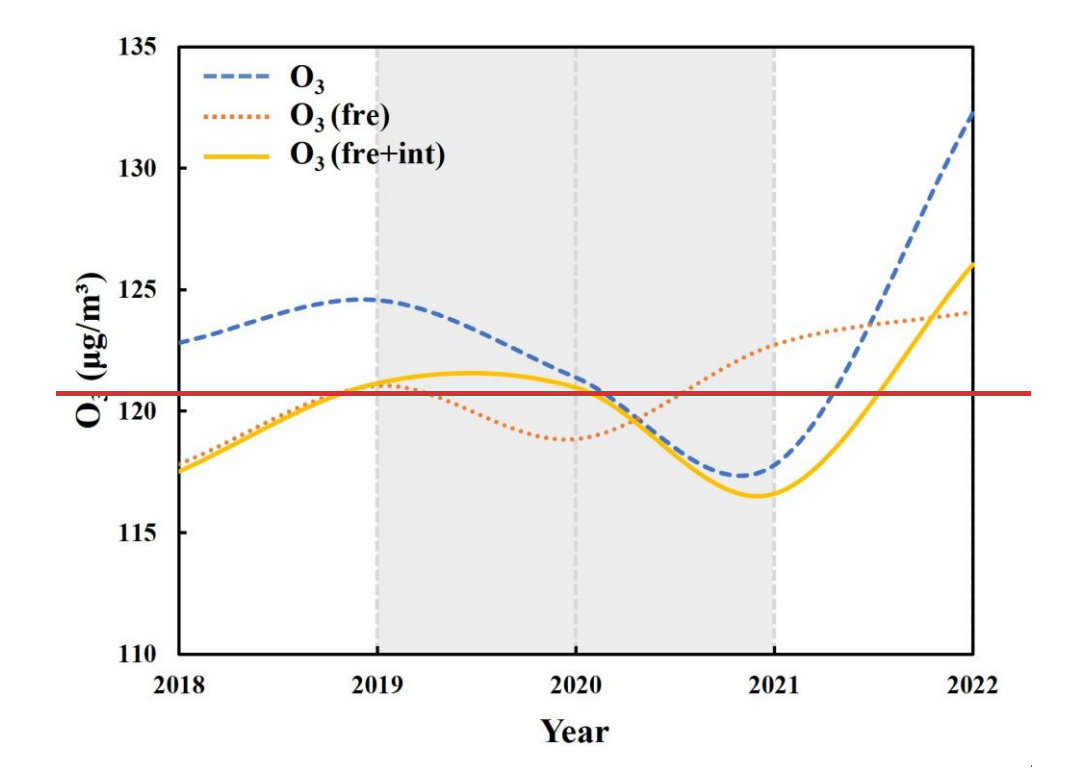
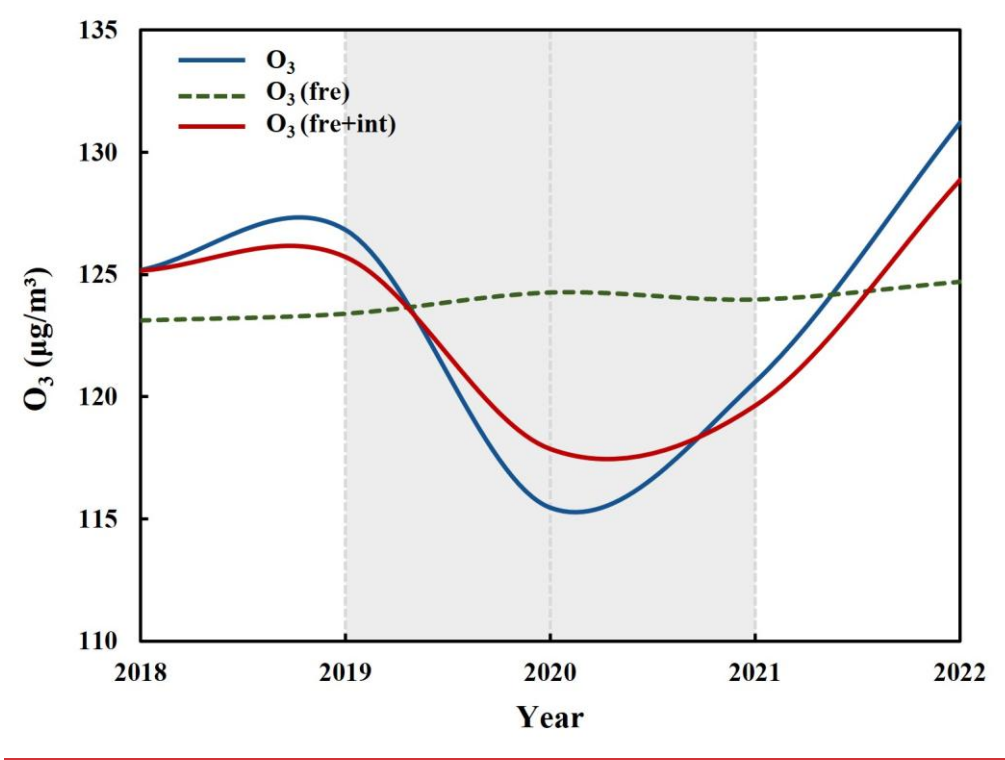


Figure 5. The average weather conditions in SWP5_C (left), SWP5_LP (middle), and SWP5_RP (right), including an 850 hPa geopotential height field superimposed on wind field (a c), sea level pressure field superimposed on 1000 hPa wind field (d-f), a 500 hPa geopotential height field superimposed on wind field (g-i). The shading represents geopotential height, black vectors represent wind and the black frame includes the YRD, and the red asterisk in (d-f) indicates the location where the TCs made landfall.





615 **Figure 6.** 2

614

617

618

619

620

621

622

Figure 6. The trend of the interannual O₃ concentration time series from June to September during 2018 to 2022 in the YRD. The blue line represents the original interannual O₃ time series, whereas the green and red lines represent the trends of reconstructed O₃ concentrations according to the frequency-only and both frequency and intensity of SWP changes, respectively. The interannual O₃-concentration trends for observed and reconstructed O₃-based on variations in SWPs in the YRD. The blue lines represent the observed interannual O₃-trend, whereas the orange and yellow lines are the trends of reconstructed O₃-concentrations according to the frequency-only and both frequency and intensity of SWP changes, respectively.

633

634

635 636

637

638

639

In reconstructing the time series of annual O₃ concentrations, we found that the definition of the SWP intensity factor played a crucial role in the reconstruction. Previous studies reconstructed the annual O₃ concentration series by defining the SWP intensity factor as either the regional mean sea level pressure or the regional minimum pressure (Hegarty et al., 2007; Liu et al., 2019). However, this definition showed poor correlation between the SWP intensity factor and the annual O₃ concentration series for certain SWPs. Therefore, we defined the SWP intensity factor for each SWP based on its specific meteorological characteristics, selecting the maximum, minimum, and mean geopotential heights across nine zones, and evaluated its validity by calculating the correlation coefficient with the annual O₃ variation series (Table 3). For SWP1 and SWP2, the maximum geopotential heights in zone 7 and zone 2 were highly correlated with the annual O₃ variation series. For SWP3 and SWP4, the minimum geopotential heights in zone 9 and zone 4 were highly correlated with the annual O₃ variation series. The maximum geopotential height reflects regional wind speeds, which determine the amount of water vapor transported into the region. Compared with SWP1, SWP2 has a larger weather system scale, so the maximum geopotential height in zone 2 shows a stronger correlation with the O3 series than that in zone 7. For SWP4, the YRD was affected by TCs, and O₃ concentrations were closely related to TC intensity. The minimum geopotential height in zone 4 reflects the TC intensity. When the SWP intensity factor was defined based on the unique meteorological characteristics of each SWP, the reconstructed series more accurately reflected the impact of changes in SWP intensity on O₃ concentrations.

<u>Table 3. Correlation coefficients between the O₃ concentration time series and different SWP intensity factors under each SWP.</u>

641

642

643

644

645

646

647

648

649

650

651

652

653 654

655

656

657

658

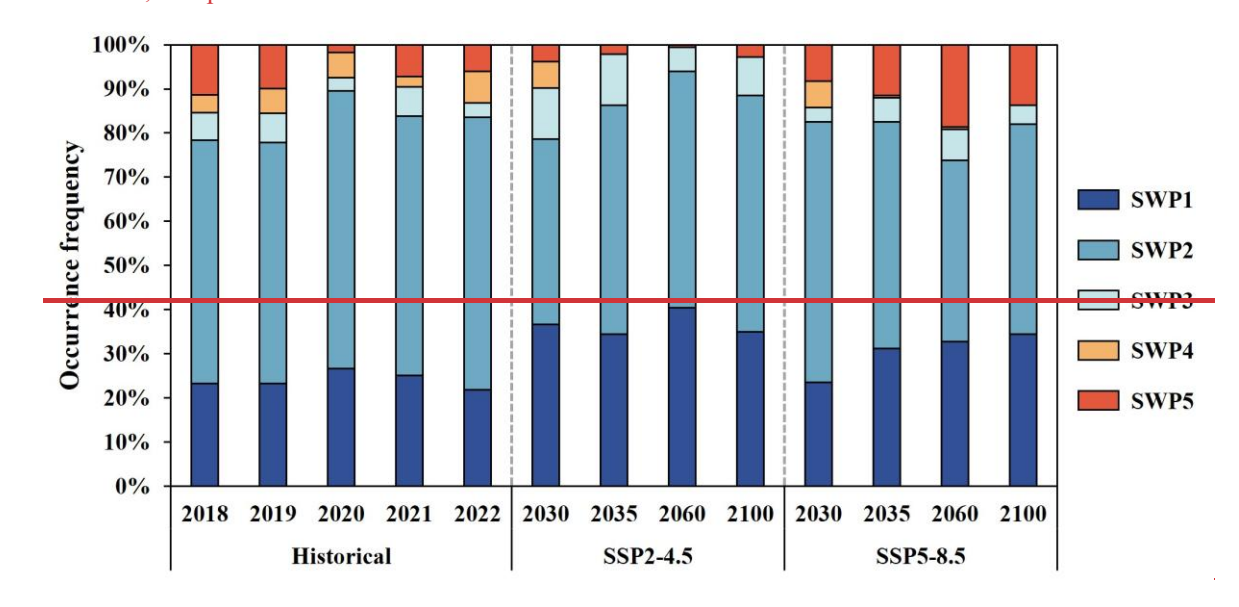
659

| | Zone 1 Type (115°~135°E, 20°~40°N) | | | | Zone 2 | | | Zone 3 | | | |
|-------------|-------------------------------------|--------------|--------------|------------------------|-----------------------|--------------|------------------------|------------------------|--------------|--------------|--------------|
| <u>Type</u> | | | | | (90°~140°E, 20°~50°N) | | | (110°~130°E, 10°~40°N) | | | |
| · | Mean | Max | Min | | Mean | Max | Min | • | Mean | Max | Min |
| SWP1 | <u>-0.62</u> | <u>-0.72</u> | <u>-0.41</u> | | <u>-0.69</u> | 0.26 | 0.45 | • | <u>-0.59</u> | <u>-0.76</u> | 0.17 |
| SWP2 | <u>-0.65</u> | <u>-0.87</u> | <u>-0.45</u> | | <u>-0.47</u> | <u>-0.88</u> | <u>-0.09</u> | | <u>-0.60</u> | <u>-0.84</u> | <u>-0.53</u> |
| SWP3 | <u>-0.41</u> | <u>-0.67</u> | 0.72 | | 0.10 | <u>-0.17</u> | 0.43 | | <u>-0.11</u> | <u>-0.60</u> | 0.75 |
| SWP4 | <u>0.15</u> | <u>-0.32</u> | 0.36 | | 0.26 | <u>0.01</u> | 0.32 | | 0.33 | <u>-0.38</u> | 0.49 |
| | <u>Zone 4</u> | | | | Zone 5 | | | Zone 6 | | | |
| Type | (110°~130°E, 25°~40°N) | | | (100°~120°E, 15°~35°N) | | | (110°~120°E, 15°~35°N) | | | | |
| | Mean | Max | Min | | Mean | Max | Min | | Mean | Max | Min |
| SWP1 | <u>-0.67</u> | <u>-0.80</u> | <u>-0.02</u> | | <u>-0.33</u> | 0.37 | 0.05 | | <u>-0.60</u> | <u>-0.82</u> | 0.10 |
| SWP2 | <u>-0.47</u> | <u>-0.73</u> | <u>-0.44</u> | | <u>-0.36</u> | <u>-0.59</u> | <u>-0.19</u> | | <u>-0.48</u> | <u>-0.65</u> | <u>-0.29</u> |
| SWP3 | <u>-0.19</u> | <u>-0.60</u> | <u>0.46</u> | | <u>0.34</u> | 0.31 | 0.67 | | 0.29 | <u>-0.29</u> | 0.85 |
| SWP4 | 0.31 | <u>-0.32</u> | <u>0.64</u> | | 0.48 | <u>-0.02</u> | <u>0.55</u> | | 0.47 | 0.26 | 0.55 |
| | Zone 7 | | | | Zone 8 | | | Zone 9 | | | |
| Type | (110°~130°E, 20°~35°N) | | | (115°~135°E, 30°~50°N) | | | (110°~130°E, 20°~40°N) | | | | |
| | Mean | Max | Min | | Mean | Max | Min | • | Mean | Max | Min |
| SWP1 | <u>-0.53</u> | <u>-0.83</u> | 0.06 | | <u>-0.40</u> | <u>-0.73</u> | 0.42 | • | <u>-0.61</u> | <u>-0.76</u> | 0.09 |
| SWP2 | <u>-0.54</u> | <u>-0.79</u> | <u>-0.25</u> | | <u>-0.31</u> | <u>-0.72</u> | 0.03 | | <u>-0.56</u> | <u>-0.77</u> | <u>-0.50</u> |
| SWP3 | 0.02 | <u>-0.69</u> | 0.86 | | <u>-0.25</u> | <u>-0.64</u> | 0.33 | | <u>-0.08</u> | <u>-0.60</u> | <u>0.87</u> |
| SWP4 | <u>0.50</u> | <u>-0.21</u> | 0.49 | | <u>-0.19</u> | <u>-0.03</u> | <u>-0.15</u> | | 0.39 | <u>-0.30</u> | 0.48 |

3.4.2 Changes in TCs and the effects on O₃ concentration over the YRD in the future

After clarifying the relationship between SWPs and O₃ pollution, future trends of O₃ concentrations under different scenarios were estimated based on projected changes in SWPs.the trend of O3 concentration change under different scenarios in the future can be estimated based on future SWP changes. Due to its unique geographical location, the YRD was subject to relatively complex weather systems. The PTT method was used to classify the weather conditions in the YRD from June to September under the SSP2-4.5 and SSP5-8.5 scenarios into four main categories. SWP1 was mainly controlled by southwesterly flow associated with the WPSH and the northeast China low, SWP2 by northwesterly flow associated with a continental high and the northeast China low, SWP3 by southeasterly flow associated with the WPSH, and SWP4 by northeasterly flow associated with the WPSH and TCs. Figure 7 illustrates the distribution of days for each SWP from June to September in the YRD during the historical period and under the SSP2-4.5 and SSP5-8.5 future scenarios. According to the average O₃ concentration of each SWP during the historical period (Table 1), SWP1 and SWP2 with higher O₃ concentrations are classified as high-average O₃ patterns. The average annual number of days during the historical period was 92.8. The high-average O₃ pattern occurred most frequently in 2022, with 98 days and higher O₃ concentrations. This confirms that changes in SWP frequency, which characterize specific O₃ concentration patterns, could influence O₃ concentration trends to a certain extent (Hegarty et al., 2007).

Under the SSP2-4.5 scenario, the frequencies of SWP1 to SWP4 were 57.79%, 19.67%, 6.76%, and 15.78%, respectively (Fig. 10). High-average O₃ pattern occurred on 93, 99, 96, and 90 days in 2030, 2035, 2060, and 2100, respectively, showing a general increasing trend, with the peak occurring in 2035. These results suggest that, considering only changes in SWP frequency, O₃ concentrations would reach a maximum in 2035 under the SSP2-4.5 scenario. Under the SSP5-8.5 scenario, the frequencies of SWP1 to SWP4 were 50.82%, 23.98%, 7.17%, and 18.03%, respectively (Fig. 10). High-average O₃ pattern will occur on 99, 90, 82, and 94 days in 2030, 2035, 2060, and 2100, respectively, under the SSP5-8.5 scenario, with the number of days increasing in 2030 and 2100. This also suggests that, considering only changes in SWP frequency, O3 concentrations would increase in 2030 and 2100 under the SSP5-8.5 scenario.O3 pollution in the YRD mostly occurs during the warm seasons (April September), so we analyzed the common SWP changes in the warm seasons of the YRD and the contribution of future SWP changes to the annual changes in O₂-concentration. Figure 7 shows the distribution of frequency of occurrence of each SWP in the warm seasons in the YRD under the historical period and the two future scenarios of SSP2 4.5 and SSP5 8.5. According to the average O₃ concentration of each SWP during the historical period, SWP1, SWP2, and SWP3 with higher O₃ concentrations are classified as high average O₃ types. The average annual number of days in the historical period is 156.6. The high average O₃ type has the highest frequency of occurrence in 2022 with higher O₃ concentrations (165 days). In the SSP2-4.5 future scenario, the high average O₃ type appears 165, 179, 182, and 178 days in 2030, 2035, 2060, and 2100, respectively, showing an upward trend of varying degrees, with the largest number of days appearing in 2060. It can be inferred that if only SWP frequency changes are considered, O3 concentration in 2060 will be higher under the SSP2 4.5 scenario. The high average O₃ type appears 157, 161, 148, and 158 days in the SSP5-8.5 future scenario in 2030, 2035, 2060, and 2100, respectively. Except for 2060, the number of days with high O₃ concentration SWPs in the YRD increases slightly. Therefore, considering only SWP frequency changes, O₃-concentration in the YRD will increase under the SSP5-8.5 scenario, except in 2060.



685

660

661

662

663

664

665

666 667

668

669 670

671

672

673

674

675

676

677

678

679

680

681

682

683

684

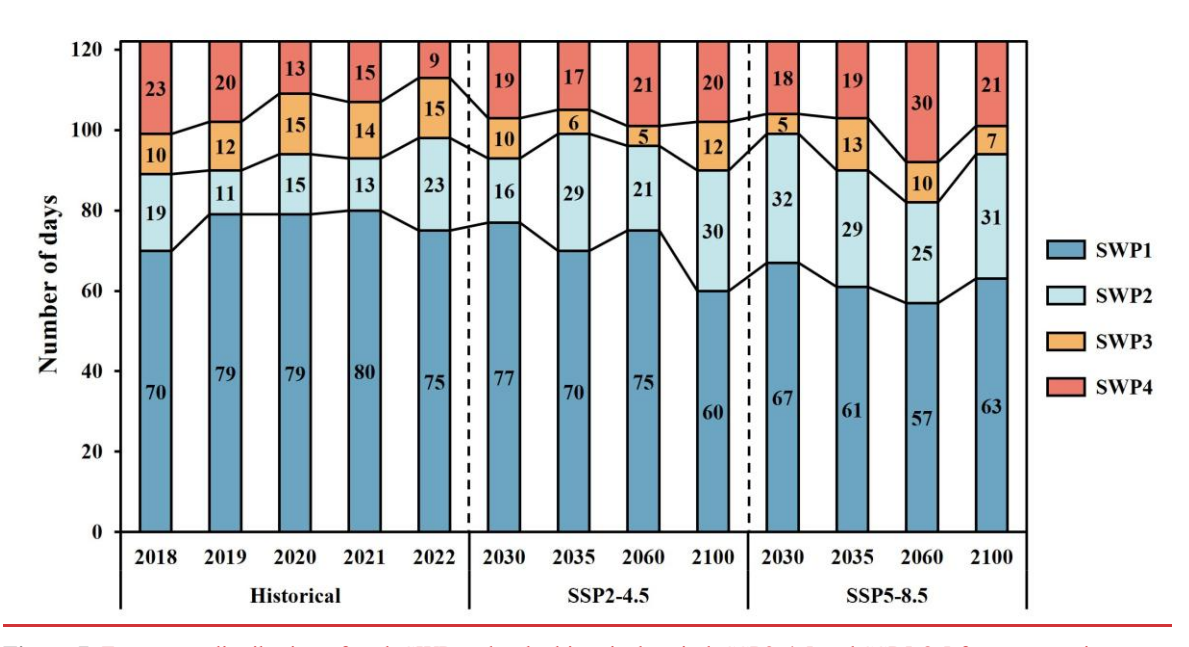


Figure 7. Frequency distribution of each SWP under the historical period, SSP2-4.5 and SSP5-8.5 future scenarios in the warm seasons over the YRD. Distribution of the number of days of occurrence of each SWP in the YRD from June to September under the historical period (2018-2022), SSP2-4.5, and SSP5-8.5 future scenarios.

688

689

690

691

692

693

694

695

696

697

698 699

700

701

702

703704

705

706

707

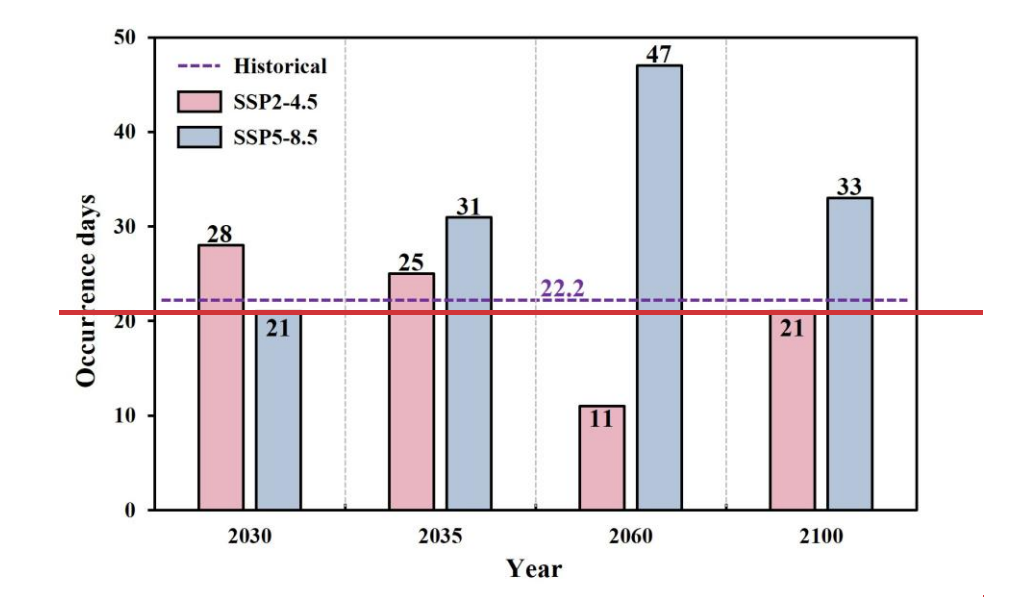
708

709

710

711

Due to the frequent occurrence of TCs in the YRD from June to September, they not only brought extreme weather events but also had a significant impact on regional O₃ pollution. We further examined changes in the number of days under the TC weather pattern (SWP4). During the historical period (2018-2022), the annual average number of days with TC weather pattern in the YRD was 16 (Fig. 8). Under the SSP2-4.5 future scenario, this number increased to 19, 17, 21, and 20 days in 2030, 2035, 2060, and 2100, respectively. This indicates that the number of days with TC weather pattern increased to varying degrees, with the lowest number of days in 2035. Under the SSP5-8.5 future scenario, this number increased to 18, 19, 30, and 24 days in 2030, 2035, 2060, and 2100, respectively. Similarly, under the SSP 5-8.5 future scenario, the number of days with the TC weather pattern in the YRD increased to varying degrees. Overall, the frequency of TCs affecting O₃ concentrations in the YRD increased significantly under both future scenarios. Due to the frequent occurrence of TCs during the warm seasons (Fig. 8), they not only bring extreme weather events but also have an important impact on regional O₃ pollution. We further studied the trend in the frequency of TC weather pattern. The SWP5 is influenced by TCs in the YRD. In the historical period (2018 2022), the average annual number of days when the TC weather pattern occurs in the YRD was 22.2 days. Under the SSP2 4.5 future scenario, there will be 28, 25, 11, and 21 days in 2030, 2035, 2060, and 2100 respectively. It can be seen that the number of days with TC weather pattern will increase to varying degrees in 2030 and 2035, while significantly decreasing in 2060. In the SSP5 8.5 future scenario, TC weather pattern will appear on 21, 31, 47, and 33 days in 2030, 2035, 2060, and 2100 respectively. Except for 2030, the number of days with SWPs controlled by TCs in the YRD will increase to varying degrees in future scenarios. Therefore, the frequency of TCs affecting O3 concentration in the YRD is expected to increase significantly in the future under the SSP5 8.5 scenario.



Historical SSP2-4.5 SSP5-8.5 Occurrence days Year

Figure 8. Occurrence days of TCs SWP under the historical period, SSP2-4.5 and SSP5-8.5 future scenarios in the YRD from June to Septemberin the warm seasons over the YRD.

3.4.3 Reconstruction of annual O₃ variability—during warm seasons—in the YRD under future scenarios

Based on the SWP classification results and the reconstructed empirical relationships, statistical projections of the annual O₃ concentration series from June to September were made for the SSP2-4.5 and SSP5-8.5 scenarios. Figure 9 compares the reconstructed annual O₃ concentration series from June to September with the historical period. When considering only changes in SWP frequency, the reconstructed O₃ series under the SSP2-4.5 scenario peaked in 2035. The reconstructed O₃ series under the SSP5-8.5 scenario increased in 2030 and 2100, consistent with the conclusions drawn in Section 3.4.2. However, overall, the reconstructed series from 2018 to 2022 indicated that changes in SWP frequency had little impact on the annual O₃ variation, and the reconstruction could not accurately capture

the actual trend. After incorporating changes in the SWP intensity factor, the reconstructed annual O_3 series more closely reflected the actual trend.

726

727

728

729

730

731

732

733

734

735

736

737

738

739

740

741

742

743

744

745

746

747

748

749

750

751

752

753

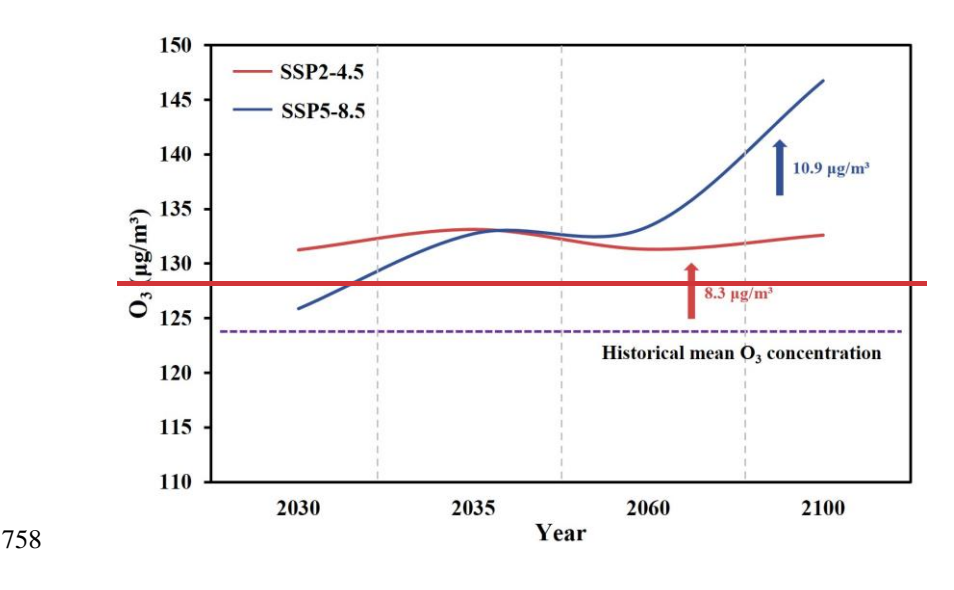
754

755

756

757

The average O₃ concentration in the YRD from June to September during 2018 to 2022 was 123.89 μg/m³. Under the SSP2-4.5 scenario, O₃ concentrations in the YRD are projected to increase relative to the historical period (Fig. 9a), with an average increase of approximately 1.88 µg/m³. Based on the reconstructed contribution of SWP changes, future O₃ concentrations in the YRD are estimated to be 2.70 μg/m³ higher than in the historical period. Under the SSP5-8.5 scenario, O₃ concentrations are projected to increase relative to the historical period (Fig. 9b), reaching 133.80 µg/m³ in 2100, an increase of approximately 6.86 μg/m³. Based on the reconstructed contribution of SWP changes, future O₃ concentrations in the YRD are estimated to be 9.85 µg/m³ higher than in the historical period. In summary, under both the SSP2-4.5 and SSP5-8.5 future climate scenarios, O3 concentrations in the YRD are projected to increase from June to September, with more severe O₃ pollution under the SSP5-8.5 scenario. Previous studies based on CMIP6 multi-model simulations have shown that surface O₃ concentrations are projected to decrease in response to reductions in anthropogenic emissions, although the magnitude and spatial distribution of changes vary among scenarios (Turnock et al., 2020; Li et al., 2023). The trends revealed in this study are generally consistent with those of previous studies, lending confidence to the robustness of our findings. According to the weather classification results and the reconstructed empirical relationship, the O₃ concentration under the two future scenarios of SSP2 4.5 and SSP5 8.5 was estimated statistically. Figure 9 shows the predicted changes in future O₃ concentration and a comparison with the average O₃ concentration in the historical period. The average O₃ concentration in the warm seasons of the YRD from 2018 to 2022 is 123.76 µg/m³. Under the SSP2 4.5 scenario, the future warm seasons O₃ concentration in the YRD will increase to varying degrees relative to the historical period, with an average increase of about 8.3 µg/m³. Under the SSP5 8.5 scenario, the warm seasons O3-concentration in the YRD will also increase to varying degrees compared with the historical period, with an average concentration increase of about 10.9 µg/m³. In particular, the warm seasons O₃ concentration in the YRD will reach 146.72 µg/m³ in 2100, which is about 23 µg/m³ higher than the average warm seasons O₃ concentration in the historical period. In summary, under the two future climate scenarios of SSP2 4.5 and SSP5 8.5, the warm seasons O₂-concentration in the YRD shows an upward trend, with O₃ pollution more severe in the SSP5 8.5 scenario. The increase in high temperature, strong solar radiation, and calm weather caused by future climate warming is conducive to the generation and accumulation of O₃. The high intensity of precursor emissions in the SSP5 8.5 scenario further aggravates O₃ pollution.



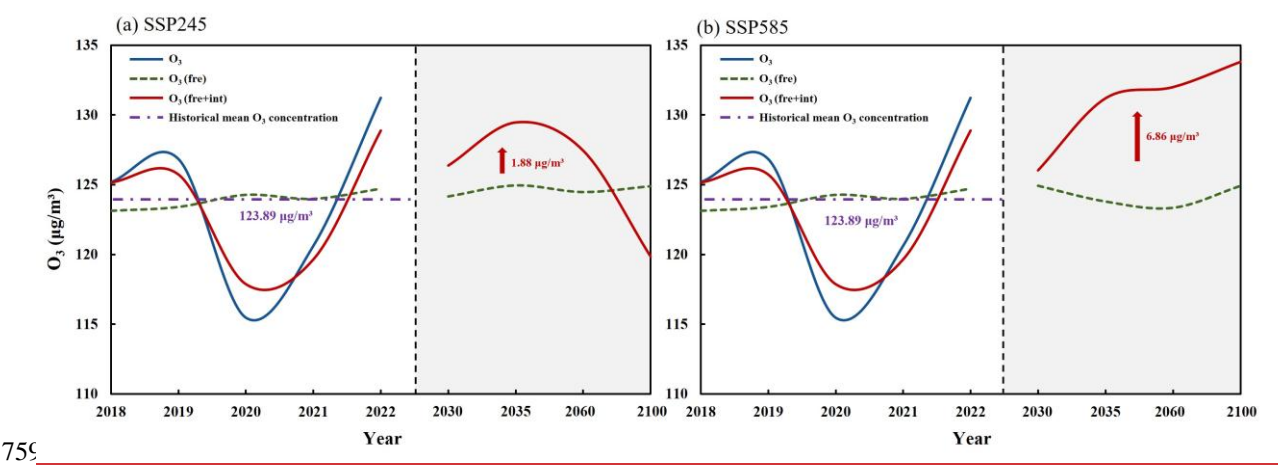
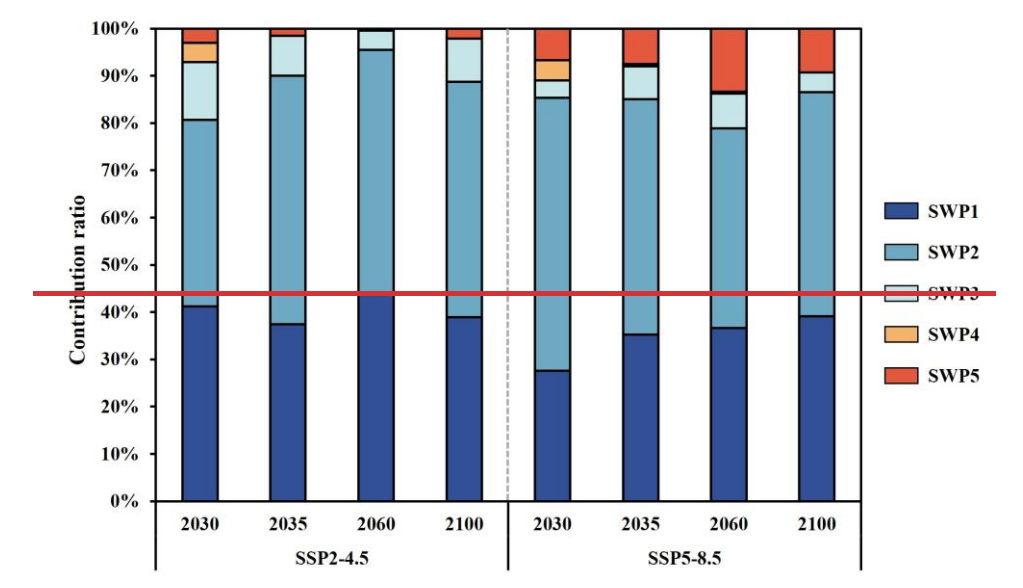


Figure 9. Estimation of O₃-concentration changes under SSP2-4.5 and SSP5-8.5 future scenarios based on intensity and frequency of SWPs, compared with the historical mean O₃-concentration. The trend of the interannual O₃ concentration time series under SSP2-4.5 (a) and SSP5-8.5 (b) future scenarios in the YRD. The blue line represents the original interannual O₃ time series, whereas the green and red lines represent the trends of reconstructed O₃ concentrations according to the frequency-only and both frequency and intensity of SWP changes, respectively.

Figure 10a shows the contribution of each SWP to the reconstructed series of future O₃ concentrations in the YRD from June to September under the SSP2-4.5 and SSP5-8.5 scenarios. We focus on the contribution of the TC weather pattern (SWP4) to the reconstructed O₃ concentration series under different scenarios (Fig. 10b). During the historical period (2018–2022), the TC weather pattern contributed an average of 13.11% to O₃ concentrations in the YRD. Under the SSP2-4.5 scenario, the contributions of the TC weather pattern in 2030, 2035, 2060, and 2100 were 15.57%, 13.93%, 17.21%, and 16.39%, respectively. The frequency of the TC weather pattern in the YRD in 2035 was lower, resulting in a lower contribution of the TC weather pattern to O₃ concentrations in that year. Under the SSP5-8.5 scenario, the TC weather pattern contributes 14.75%, 15.57%, 24.59%, and 19.67% to O₃ changes in 2030, 2035, 2060, and 2100, respectively. Under both the SSP2-4.5 and SSP5-8.5 scenarios, the contribution of the TC weather pattern to O₃ pollution increases to varying degrees compared with the historical period. This suggests that under future climate change, the impact of TC weather pattern on O₃ pollution in the YRD may intensify. Further research is needed on the relationship between key

SWPs, such as TC weather pattern, and O₃ formation mechanisms to more accurately predict and mitigate regional O₃ pollution under future climate conditions. We focus on the contribution of the TC weather pattern to the O₃-concentration under different future scenarios. Figure 10 shows the estimated contribution of each SWP to the future O₃-concentration. The SWP5 is influenced by TCs in the YRD. In the historical period (2018-2022), the average contribution of TCs to the warm seasons O₃-concentration in the YRD was 10.95%. Under the SSP2-4.5 scenario, the contribution of the TC weather pattern in 2030, 2035, 2060, and 2100 was 15.14, 9.97, 4.50, and 11.27%, respectively. Among them, the frequency of days controlled by the TC weather pattern in the YRD in 2060 was relatively low, resulting in a relatively low contribution of the TC weather pattern to the O₃-concentration in that year. Under the SSP5-8.5 scenario, the contribution of the TC weather pattern in 2030, 2035, 2060, and 2100 was 10.31, 14.50, 20.66 and 13.48%, respectively. It can be seen that under this scenario, except for 2030, the contribution of the TC weather pattern will increase to varying degrees compared with the historical period, that is, the TC weather pattern will have a significant impact on O₃ pollution in the YRD under this scenario.



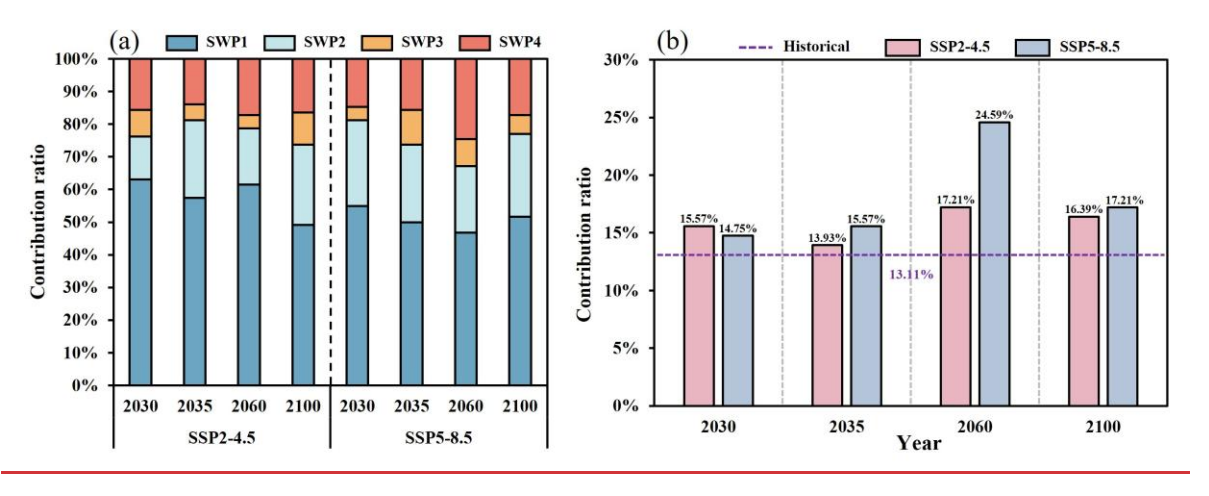


Figure 10. Contribution ratio of different SWPs to predicted O₃ concentrations under SSP2 4.5 and SSP5 8.5 future scenarios. Contribution of SWP to the projected annual variation series of O₃ concentration under the SSP2-4.5 and SSP5-8.5 future scenarios. (a) Contribution of four SWPs, (b) Contribution of TC weather pattern (SWP4).

4 Conclusions

797

798

799 800

801 802

803

804

805

806

807

808

809

810

811

812

813

814

815

816817

818

819

820

821

822

823 824

825

826

827

828

829

830

831

832

833

834

835

836

837

838

839

This study investigates the impact of meteorological conditions on O₃ pollution and future trends in the YRD, with a particular focus on the influence and mechanisms of TCs on O₃ pollution. In response to the problem of O₃ pollution in the YRD, this paper studies the impact of weather conditions on O₃ pollution and future trends in the YRD, with special attention to the impact and mechanism of TCs on Θ_3 pollution. The spatial distribution and temporal variation of O_3 pollution during TC events in the YRD from 2018 to 2022 were analyzed. The spatial distribution characteristics of O₃ pollution and the changing characteristics during TC activity in the YRD from 2018 to 2022 were analyzed. The PTT objective classification method was applied to identify the main SWPs in the YRD from June to September 2018-2022 and assess their influence on varying levels of O₃ pollution. Finally, using the reconstructed empirical relationship, the annual variation of O₃ concentrations in the YRD from June to September under future scenarios was statistically projected, and the contribution of TCs to future O₃ changes was quantified. The main SWPs in the YRD and their impact on varying levels of O₃ pollution were discussed using the PTT objective classification method. Finally, based on the reconstructed empirical relationship, the warm seasons O₃ concentration in the YRD under future scenarios was statistically estimated, and the contribution of TCs to future O₂-concentration changes. The main findings are summarized as follows.

Analysis of O₃ pollution characteristics in the YRD from 2018 to 2022 indicates that inter-month variations of O₃ concentrations exhibit an M-shaped patternAnalysis of O₃ pollution characteristics in the YRD from 2018 to 2022 shows that, affected by changes in temperature, solar radiation, and precipitation, inter month variations of O₂ concentrations present an M shaped pattern. Peaks generally occur in June and September, with O₃ concentrations showing substantial fluctuations during summer. Peaks generally occurring in June and September, and O₂-concentrations fluctuate greatly in summer. During TC activity from 2018 to 2022, O₃ pollution in typical YRD cities exhibited similar temporal trends, generally increasing initially and then decreasing, closely associated with the trajectory and center position of the TCs.O₃ pollution in typical cities in the YRD during TC activity between 2018 and 2022 showed similar temporal variation trends, usually showing a pattern of first increasing and then decreasing, which is closely related to the path and center location of the TCs. When the TC center approaches the YRD, regional O₃ concentrations decrease due to strong winds and rainfall, facilitating atmospheric pollutant removal. When the TCs center is close to the YRD, the O₂-concentration in the region will decrease due to strong winds and rainfall, which is conducive to the removal of pollutants in the atmosphere. Conversely, when TCs are in their formation or dissipation stages, or their peripheral airflows influence the YRD, high temperatures, clear skies, and dry conditions favor O₃ formation and accumulation. On the contrary, when the TCs are in the formation or dissipation stage, or their periphery airflows affecting the YRD, high temperature, sunny, and dry climate conditions are conducive to the formation and accumulation of O₃.

Using the PTT objective classification method, four main SWPs were identified in the YRD from June to September 2018–2022. SWP1 is mainly controlled by the southwesterly flow introduced by the WPSH and the northeast China low, SWP2 by northwesterly flow introduced by a continental high and the northeast China low, SWP3 by southeasterly flow introduced by the WPSH, and SWP4 by northeasterly flow introduced by the WPSH and TCs. SWP1 is the dominant SWP, occurring 62.79 % of the time, whereas the TC weather pattern (SWP4) occurs 13.11 % of the time. SWP2 is influenced by dry northwesterly flow, exhibiting lower humidity (76.74 %) and slower wind speeds (2.03 m/s), which

hinder pollutant dispersion and lead to higher O₃ concentrations. Under SWP4, TCs bring strong winds and rainstorms, increase humidity (80.03%), and enhance wind speeds (2.64 m/s), resulting in lower average O₃ concentrations. Through the PTT objective weather classification method, five dominant SWPs in the YRD were identified. SWP1 is mainly controlled by continental high and northeastern China low in the YRD, SWP2 is mainly controlled by the WPSH and southwest vortex, SWP3 is mainly controlled by the WPSH, SWP4 is mainly controlled by a saddle pattern pressure field, and SWP5 is mainly controlled by the WPSH and TCs. Among them, the high temperature in the region under SWP2 intensifies the photochemical reaction, and the south wind brings pollutants from the PRD, resulting in the highest O₃ concentration under SWP2. The average O₃ concentration under SWP5 is second high, mainly because the prevailing downdrafts controlled by the WPSH are strengthened due to TC activities, making the atmosphere more stagnant and affecting photochemical reactions and the transport and diffusion of pollutants.

To investigate the interaction mechanisms between TC weather patterns and O3 pollution, three pollution levels, clean type (C), local pollution (LP), and regional pollution (RP), were defined based on O₃ characteristics, and the corresponding atmospheric circulation features were analyzed in detail. For SWP4 C, TCs make landfall in the YRD, bringing strong winds and rainstorms that inhibit O3 accumulation and maintain clean air conditions. In contrast, under the SWP4 LP and SWP4 RP, downdrafts induced by the peripheral airflows of TCs that have not yet made landfall led to more stagnant atmospheric conditions. Elevated temperatures and weak winds over the YRD create conditions highly favorable for O₃ formation. The mean O₃ concentrations for these three categories were 93.46 μg/m³, 126.97 μg/m³, and 161.19 μg/m³. The clean type occurred more than half the time, contributing to the lower mean O₃ concentration (115.07 µg/m³) under the SWP4. When the TC centers are located at 130°-135°E and 20°-30°N, the YRD is influenced by downdrafts from the peripheral flows of the TCs, facilitating the formation of high-concentration O₃ pollution. The TC weather pattern (SWP5) is a highfrequency weather pattern in summer, with an occurrence frequency of 72.22%. The meteorological conditions of high temperature, low humidity, and strong solar radiation are conducive to the occurrence of photochemical reactions. For SWP5 LP and SWP5 RP, the prevailing downdrafts controlled by the WPSH will be strengthened by the TCs activities, making the air calm and stagnant, and the meteorological conditions of high temperature and low humidity will appear, causing the outbreak of O₃ pollution in the YRD. When the center of the TCs is located at 130°-135°E, 20°-30°N, the YRD is affected by the downdrafts outside the TCs, and high concentration O₃ pollution is prone to form.

The SWP intensity and frequency contribute 10.05% and 69.66% to the annual O₃ variation series, respectively. Compared to frequency, intensity variations have a more significant impact on O₃ variation. Classification of SWPs from June to September under the SSP2-4.5 and SSP5-8.5 future scenarios shows that the number of days with TC weather pattern has increased to varying degrees, and the duration of TCs impacts will increase in the future. SWP intensity factors are defined based on the meteorological characteristics and location of each SWP, and a statistical estimate of the O₃ concentration variation series from June to September in the YRD under future scenarios is made using data reconstruction methods. Under the SSP2-4.5 and SSP5-8.5 future scenarios, O₃ concentrations increase by an average of 1.88 μg/m³ and 6.86 μg/m³ compared to the historical period. Based on their reduction contributions, the increase is expected to be 2.70 μg/m³ and 9.85 μg/m³. Under the two future scenarios, the contribution of TC weather pattern to O₃ pollution has increased to varying degrees compared with the historical period, indicating that the impact of TC weather pattern on O₃ pollution in the YRD may be further intensified in the future. Based on data reconstruction, a statistical estimate of the warm seasons O₃

concentration in the YRD under future scenarios was made. Under the SSP2 4.5 scenario, it is estimated that the average O_3 concentration in the YRD in the future will be 8.3 μ g/m³ higher than in the historical period. Among them, the TC weather pattern contributes the most to the change in O_3 concentration in 2030, reaching 15.14%. Under the SSP5 8.5 scenario, the average concentration will increase by about 10.9 μ g/m³, especially by 2100, it is expected to be about 23 μ g/m³ higher than the current situation. In addition, the contribution of TC weather pattern to O_3 pollution is expected to increase under the SSP5-8.5 scenario, among which the contribution in 2060 will be the highest, reaching 20.66%. This indicates that under the scenario of intensified climate change, TC weather pattern will have a more significant impact on O_3 -pollution in the YRD.

In summary, O₃ pollution in the YRD is on the rise, and summer O₃ pollution is often related to TC activities, and often occurs before and after TC activities. Through the research of this article, we have deepened our understanding of the mechanism of TCs on regional O₃ pollution. In addition, under the background of global warming, the intensity and duration of TC generation will increase, which will have a serious impact on China's coastal areas. Compared with the direct damage caused by landfalling TCs, the secondary disasters caused by them, such as O₃ pollution, should also be taken seriously. The research results have important scientific significance and practical application value for the in-depth understanding of the formation mechanism of O₃ pollution in the YRD, formulating targeted pollution prevention and control strategies, and improving regional air quality.

| 902 | Data availability. Chinese O ₃ monitoring data are available at http://www.cnemc.cn/en/ . Meteorological |
|-----|---|
| 903 | data are available at http://rda.ucar.edu/datasets/ds083.2/ . The TCs trajectory dataset are available at |
| 904 | https://www.typhoon.org.cn/. CMIP6 future climate scenario data are available at |
| 905 | https://www.scidb.cn/detail?dataSetId=791587189614968832. |
| 906 | |
| 907 | Author contributions. MiX had the original ideas, MeX and YL collected and processed the data, |
| 908 | designed the research and prepared the original draft. MiX discuss the results and revise the original draft |
| 909 | and also provided financial support for the project leading to this publication. DM revised the paper and |
| 910 | helped to collect the data. LF, SZ, and SC checked the English of the original paper. MiX had the original |
| 911 | idea for the study, designed the experiments. MeX, DG, and DM collected and processed the data, |
| 912 | designed the research and prepared the original draft. MiX discuss the results and revise the original draft |
| 913 | and also provided financial support for the project leading to this publication. YL revised the paper and |
| 914 | helped to collect the data. LF, SC, and SZ checked the English of the original paper. |
| 915 | |
| 916 | Competing interests. The contact author has declared that none of the authors has any competing interests. |
| 917 | |
| 918 | Financial support. This research has been supported by the National Nature Science Foundation of China |
| 919 | (42275102), the Special Science and Technology Innovation Program for Carbon Peak and Carbon |
| 920 | Neutralization of Jiangsu Province (BE2022612), the National Key Basic Research Development |
| 921 | Program of China (2024YFC3711905) and the research start-up fund for the introduction of talents from |
| 922 | Nanjing Normal University (184080H201B57). |
| 923 | |

- 924 References
- Adak, S., Mandal, N., Mukhopadhyay, A., Maity, P. P., and Sen, S.: Current state and prediction of future
- global climate change and variability in terms of CO₂ levels and temperature, in: Enhancing resilience
- 927 of dryland agriculture under changing climate: Interdisciplinary and convergence Approaches,
- 928 Springer, 15-43, 10.1007/978-981-19-9159-2 2, 2023.
- 929 Akritidis, D., Pozzer, A., and Zanis, P.: On the impact of future climate change on tropopause folds and
- 930 tropospheric ozone, Atmospheric Chemistry and Physics, 19, 14387-14401,
- 931 http://doi.org/10.5194/acp-19-14387-2019, 2019.
- 932 Arnold, S. R., Lombardozzi, D., Lamarque, J. F., Richardson, T., Emmons, L. K., Tilmes, S., Sitch, S. A.,
- 933 Folberth, G., Hollaway, M. J., and Martin, M. V.: Simulated Global Climate Response to Tropospheric
- Ozone-Induced Changes in Plant Transpiration, Geophysical Research Letters, 45, 13070-13079,
- 935 <u>http://doi.org/10.1029/2018gl079938</u>, 2018.
- 936 Balaguru, K., Chang, C. C., Leung, L. R., Foltz, G. R., Hagos, S. M., Wehner, M. F., Kossin, J. P., Ting,
- 937 M. F., and Xu, W. W.: A Global Increase in Nearshore Tropical Cyclone Intensification, Earths Future,
- 938 12, http://doi.org/10.1029/2023ef004230, 2024.
- Bao, Q. Y., Lin, W. L., Jin, J. L., Xu, X. B., Zhao, G., Zhang, X. Y., and Ma, Q. L.: Long-term variation
- of O₃ in the Yangtze River Delta and its influencing factors from a regional perspective, Urban Climate,
- 941 60, http://doi.org/10.1016/j.uclim.2025.102353, 2025.
- 942 Bhatia, K., Baker, A., Yang, W. C., Vecchi, G., Knutson, T., Murakami, H., Kossin, J., Hodges, K., Dixon,
- K., Bronselaer, B., and Whitlock, C.: A potential explanation for the global increase in tropical cyclone
- rapid intensification, Nature Communications, 13, http://doi.org/10.1038/s41467-022-34321-6, 2022.
- Chand, S. S., Walsh, K. J. E., Camargo, S. J., Kossin, J. P., Tory, K. J., Wehner, M. F., Chan, J. C. L.,
- Klotzbach, P. J., Dowdy, A. J., Bell, S. S., Ramsay, H. A., and Murakami, H.: Declining tropical
- 947 cyclone frequency under global warming, Nature Climate Change, 12, 655-+,
- 948 http://doi.org/10.1038/s41558-022-01388-4, 2022.
- 949 Chen, L., Zhu, J., Liao, H., Yang, Y., and Yue, X.: Meteorological influences on PM_{2.5} and O₃ trends and
- associated health burden since China's clean air actions, Science of the Total Environment, 744,
- 951 http://doi.org/10.1016/j.scitotenv.2020.140837, 2020.
- 952 Chow, E. C. H., Li, R. C. Y., and Zhou, W.: Influence of Tropical Cyclones on Hong Kong Air Quality,
- 953 Advances in Atmospheric Sciences, 35, 1177-1188, http://doi.org/10.1007/s00376-018-7225-4, 2018.
- Chu, J. E., Lee, S. S., Timmermann, A., Wengel, C., Stuecker, M. F., and Yamaguchi, R.: Reduced tropical
- cyclone densities and ocean effects due to anthropogenic greenhouse warming, Science Advances, 6,
- 956 http://doi.org/10.1126/sciadv.abd5109, 2020.
- 957 Deng, T., Wang, T. J., Wang, S. Q., Zou, Y., Yin, C. Q., Li, F., Liu, L., Wang, N., Song, L., Wu, C., and
- Wu, D.: Impact of typhoon periphery on high ozone and high aerosol pollution in the Pearl River Delta
- 959 region, Science of the Total Environment, 668, 617-630,
- 960 http://doi.org/10.1016/j.scitotenv.2019.02.450, 2019.
- 961 Fu, Y. and Tai, A. P. K.: Impact of climate and land cover changes on tropospheric ozone air quality and
- public health in East Asia between 1980 and 2010, Atmospheric Chemistry and Physics, 15, 10093-
- 963 10106, http://doi.org/10.5194/acp-15-10093-2015, 2015.
- 964 Gao, D., Xie, M., Liu, J., Wang, T. J., Ma, C. Q., Bai, H. K., Chen, X., Li, M. M., Zhuang, B. L., and Li,
- S.: Ozone variability induced by synoptic weather patterns in warm seasons of 2014-2018 over the
- 966 Yangtze River Delta region, China, Atmospheric Chemistry and Physics, 21, 5847-5864,
- 967 <u>http://doi.org/10.5194/acp-21-5847-2021</u>, 2021.

- 968 Gong, S. L., Zhang, L., Liu, C., Lu, S. H., Pan, W. J., and Zhang, Y. H.: Multi-scale analysis of the
- impacts of meteorology and emissions on PM_{2.5} and O₃ trends at various regions in China from 2013
- 970 to 2020 2. Key weather elements and emissions, Science of the Total Environment, 824,
- 971 http://doi.org/10.1016/j.scitotenv.2022.153847, 2022.
- Gong, X., Sun, F. X., Wei, L., Zhang, Y., Xia, M. J., Ge, M., and Xiong, L. L.: Association of Ozone and
- 973 Temperature with Ischemic Heart Disease Mortality Risk: Mediation and Interaction Analyses,
- 974 Environmental Science & Technology, 58, 20378-20388, http://doi.org/10.1021/acs.est.4c05899, 2024.
- Hegarty, J., Mao, H., and Talbot, R.: Synoptic controls on summertime surface ozone in the northeastern
- 976 United States, Journal of Geophysical Research-Atmospheres, 112,
- 977 <u>http://doi.org/10.1029/2006jd008170</u>, 2007.
- Hou, X. W., Zhu, B., Kumar, K. R., and Lu, W.: Inter-annual variability in fine particulate matter pollution
- over China during 2013-2018: Role of meteorology, Atmospheric Environment, 214,
- 980 <u>http://doi.org/10.1016/j.atmosenv.2019.116842</u>, 2019.
- 981 Hu, W. Z., Liu, R., Chen, Z. C., Ouyang, S. S., Hu, T. T., Wang, Y., Cui, Z. Y., Jiang, B., Chen, D. H.,
- and Liu, S. C.: Processes conducive to high ozone formation in Pearl River Delta in the presence of
- 983 Pacific tropical cyclones, Atmospheric Environment, 307,
- 984 http://doi.org/10.1016/j.atmosenv.2023.119859, 2023.
- 985 Huth, R., Beck, C., and Kucerová, M.: Synoptic-climatological evaluation of the classifications of
- atmospheric circulation patterns over Europe, International Journal of Climatology, 36, 2710-2726,
- 987 http://doi.org/10.1002/joc.4546, 2016.
- 988 Jiang, Y. C., Zhao, T. L., Liu, J., Xu, X. D., Tan, C. H., Cheng, X. H., Bi, X. Y., Gan, J. B., You, J. F., and
- 289 Zhao, S. Z.: Why does surface ozone peak before a typhoon landing in southeast China?, Atmospheric
- 990 Chemistry and Physics, 15, 13331-13338, http://doi.org/10.5194/acp-15-13331-2015, 2015.
- 991 Jung, H.: Humans fuel stronger cyclones, Nature Climate Change, 15, 351-351,
- 992 http://doi.org/10.1038/s41558-025-02321-1, 2025.
- 993 Keeble, J., Bednarz, E. M., Banerjee, A., Abraham, N. L., Harris, N. R. P., Maycock, A. C., and Pyle, J.
- A.: Diagnosing the radiative and chemical contributions to future changes in tropical column ozone
- 995 with the UM-UKCA chemistry-climate model, Atmospheric Chemistry and Physics, 17, 13801-13818,
- 996 http://doi.org/10.5194/acp-17-13801-2017, 2017.
- 997 Kossin, J. P.: A global slowdown of tropical-cyclone translation speed, Nature, 558, 104-+,
- 998 <u>http://doi.org/10.1038/s41586-018-0158-3</u>, 2018.
- 999 Lam, K. S., Wang, T. J., Wu, C. L., and Li, Y. S.: Study on an ozone episode in hot season in Hong Kong
- and transboundary air pollution over Pearl River Delta region of China, Atmospheric Environment,
- 39, 1967-1977, http://doi.org/10.1016/j.atmosenv.2004.11.023, 2005.
- Li, H., Yang, Y., Jin, J., Wang, H., Li, K., Wang, P., and Liao, H.: Climate-driven deterioration of future
- ozone pollution in Asia predicted by machine learning with multi-source data, Atmospheric Chemistry
- and Physics, 23, 1131-1145, http://doi.org/10.5194/acp-23-1131-2023, 2023.
- Li, K., Jacob, D. J., Shen, L., Lu, X., De Smedt, I., and Liao, H.: Increases in surface ozone pollution in
- 1006 China from 2013 to 2019: anthropogenic and meteorological influences, Atmospheric Chemistry and
- 1007 Physics, 20, 11423-11433, http://doi.org/10.5194/acp-20-11423-2020, 2020.
- 1008 Li, S., Gao, Y., Zhang, J., Hong, C., Zhang, S., Chen, D., Wild, O., Feng, Z., Xu, Y., and Guo, X.:
- Mitigating climate change and ozone pollution will improve Chinese food security, One Earth,
- 1010 <u>http://doi.org/10.1016/j.oneear.2024.12.002</u>, 2024.
- 1011 Liu, J. D., Wang, L. L., Li, M. G., Liao, Z. H., Sun, Y., Song, T., Gao, W. K., Wang, Y. H., Li, Y., Ji, D.

- 1012 S., Hu, B., Kerminen, V. M., Wang, Y. S., and Kulmala, M.: Quantifying the impact of synoptic
- circulation patterns on ozone variability in northern China from April to October 2013-2017,
- 1014 Atmospheric Chemistry and Physics, 19, 14477-14492, http://doi.org/10.5194/acp-19-14477-2019,
- 1015 2019.
- 1016 Lu, H. X., Lyu, X. P., Cheng, H. R., Ling, Z. H., and Guo, H.: Overview on the spatial-temporal
- 1017 characteristics of the ozone formation regime in China, Environmental Science-Processes & Impacts,
- 1018 21, 916-929, http://doi.org/10.1039/c9em00098d, 2019.
- 1019 Moon, M., Min, S. K., Chu, J. E., An, S. I., Son, S. W., Ramsay, H., and Wang, Z.: Tropical cyclone
- 1020 response to ambitious decarbonization scenarios, Npj Climate and Atmospheric Science, 8,
- 1021 http://doi.org/10.1038/s41612-025-01122-9, 2025.
- 1022 Moon, M., Ha, K. J., Kim, D., Ho, C. H., Park, D. S. R., Chu, J. E., Lee, S. S., and Chan, J. C. L.: Rainfall
- strength and area from landfalling tropical cyclones over the North Indian and western North Pacific
- 1024 oceans under increased CO2 conditions, Weather and Climate Extremes, 41,
- 1025 http://doi.org/10.1016/j.wace.2023.100581, 2023.
- 1026 Philipp, A., Beck, C., Huth, R., and Jacobeit, J.: Development and comparison of circulation type
- 1027 classifications using the COST 733 dataset and software, International Journal of Climatology, 36,
- 1028 2673-2691, http://doi.org/10.1002/joc.3920, 2016.
- 1029 Qi, C. N., Wang, P. Y., Yang, Y., Li, H. M., Zhang, H., Ren, L. L., Jin, X. P., Zhan, C. C., Tang, J. P., and
- Liao, H.: Impacts of tropical cyclone-heat wave compound events on surface ozone in eastern China:
- 1031 comparison between the Yangtze River and Pearl River deltas, Atmospheric Chemistry and Physics,
- 24, 11775-11789, http://doi.org/10.5194/acp-24-11775-2024, 2024.
- Saunier, A., Ormeño, E., Piga, D., Armengaud, A., Boissard, C., Lathière, J., Szopa, S., Genard-Zielinski,
- 1034 A. C., and Fernandez, C.: Isoprene contribution to ozone production under climate change conditions
- in the French Mediterranean area, Regional Environmental Change, 20
- 1036 http://doi.org/10.1007/s10113-020-01697-4, 2020.
- 1037 Shu, L., Xie, M., Gao, D., Wang, T. J., Fang, D. X., Liu, Q., Huang, A. N., and Peng, L. W.: Regional
- severe particle pollution and its association with synoptic weather patterns in the Yangtze River Delta
- region, China, Atmospheric Chemistry and Physics, 17, 12871-12891, http://doi.org/10.5194/acp-17-
- 1040 12871-2017, 2017.
- Shu, L., Xie, M., Wang, T. J., Gao, D., Chen, P. L., Han, Y., Li, S., Zhuang, B. L., and Li, M. M.: Integrated
- studies of a regional ozone pollution synthetically affected by subtropical high and typhoon system in
- the Yangtze River Delta region, China, Atmospheric Chemistry and Physics, 16, 15801-15819,
- 1044 http://doi.org/10.5194/acp-16-15801-2016, 2016.
- Turnock, S. T., Allen, R. J., Andrews, M., Bauer, S. E., Deushi, M., Emmons, L., Good, P., Horowitz, L.,
- John, J. G., Michou, M., Nabat, P., Naik, V., Neubauer, D., O'Connor, F. M., Olivié, D., Oshima, N.,
- 1047 Schulz, M., Sellar, A., Shim, S., Takemura, T., Tilmes, S., Tsigaridis, K., Wu, T., and Zhang, J.:
- Historical and future changes in air pollutants from CMIP6 models, Atmos. Chem. Phys., 20, 14547-
- 1049 14579, http://doi.org/10.5194/acp-20-14547-2020, 2020.
- Wang, G. H., Wu, L. W., Mei, W., and Xie, S. P.: Ocean currents show global intensification of weak
- tropical cyclones, Nature, 611, 496-+, http://doi.org/10.1038/s41586-022-05326-4, 2022a.
- Wang, J. H., Wang, P., Tian, C. F., Gao, M., Cheng, T. T., and Mei, W.: Consecutive Northward Super
- 1053 Typhoons Induced Extreme Ozone Pollution Events in Eastern China, Npj Climate and Atmospheric
- Science, 7, http://doi.org/10.1038/s41612-024-00786-z, 2024a.
- 1055 Wang, N., Huang, X., Xu, J. W., Wang, T., Tan, Z. M., and Ding, A. J.: Typhoon-boosted biogenic

- emission aggravates cross-regional ozone pollution in China, Science Advances, 8, http://doi.org/10.1126/sciadv.abl6166, 2022b.
- 1058 Wang, N., Wang, H. Y., Huang, X., Chen, X., Zou, Y., Deng, T., Li, T. Y., Lyu, X., and Yang, F. M.:
- Extreme weather exacerbates ozone pollution in the Pearl River Delta, China: role of natural processes,
- 1060 Atmospheric Chemistry and Physics, 24, 1559-1570, http://doi.org/10.5194/acp-24-1559-2024, 2024b.
- Wang, S., Murakami, H., and Cooke, W. F.: Anthropogenic forcing changes coastal tropical cyclone
- frequency, Npj Climate and Atmospheric Science, 6, http://doi.org/10.1038/s41612-023-00516-x,
- 1063 2023a.
- 1064 Wang, Y., Yang, Y. J., Yuan, Q. Q., Li, T. W., Zhou, Y., Zong, L., Wang, M. Y., Xie, Z. Y., Ho, H. C., Gao,
- 1065 M., Tong, S. L., Lolli, S., and Zhang, L. P.: Substantially underestimated global health risks of current
- ozone pollution, Nature Communications, 16, http://doi.org/10.1038/s41467-024-55450-0, 2025.
- Wang, Y. T., Zhao, Y., Liu, Y. M., Jiang, Y. Q., Zheng, B., Xing, J., Liu, Y., Wang, S., and Nielsen, C. P.:
- Sustained emission reductions have restrained the ozone pollution over China, Nature Geoscience, 16,
- 967-+, http://doi.org/10.1038/s41561-023-01284-2, 2023b.
- 1070 Wu, L. G., Yu, R. L., Xiang, C. Y., Yu, H., Feng, Y. C., and Zhou, X. Y.: Extreme Impacts of Four
- 1071 Landfalling Tropical Cyclones in China during the 2024 Peak Season, Advances in Atmospheric
- 1072 Sciences, 42, 817-824, http://doi.org/10.1007/s00376-025-4465-y, 2025.
- 1073 Wu, S. H.: Research progress in climate change impact, risk, and adaptation: An interpretation of Part 2
- 1074 of China's
- 1075 Fourth National Assessment Report on Climate Change., China Population, Resources and Environment,
- 1076 33, 80-86, 2023.
- 1077 Xi, M., Luo, Y., Li, Y., Ma, D., Feng, L., Zhang, S., Chen, S., and Xie, M.: Comprehensive analysis of
- prevailing weather patterns and high-impact typhoon tracks to reveal where and how tropical cyclone
- affects regional ozone pollution in the Yangtze River Delta region, China, Atmospheric Environment,
- 1080 361, 121498, http://doi.org/https://doi.org/10.1016/j.atmosenv.2025.121498, 2025.
- 1081 Xie, M., Zhu, K. G., Wang, T. J., Chen, P. L., Han, Y., Li, S., Zhuang, B. L., and Shu, L.: Temporal
- 1082 characterization and regional contribution to O₃ and NO_x at an urban and a suburban site in Nanjing,
- 1083 China, Science of the Total Environment, 551, 533-545, http://doi.org/10.1016/j.scitotenv.2016.02.047,
- 1084 2016.
- 1085 Xu, J. W., Zhou, D. R., Gao, J., Huang, X., Xue, L. K., Huo, J. T., Fu, Q. Y., and Ding, A. J.: Biogenic
- emissions-related ozone enhancement in two major city clusters during a typical typhoon process,
- 1087 Applied Geochemistry, 152, http://doi.org/10.1016/j.apgeochem.2023.105634, 2023a.
- 1088 Xu, Y. F., Shen, A., Jin, Y. B., Liu, Y. M., Lu, X., Fan, S. J., Hong, Y. Y., and Fan, Q.: A quantitative
- assessment and process analysis of the contribution from meteorological conditions in an O3 pollution
- 1090 episode in Guangzhou, China, Atmospheric Environment, 303,
- 1091 http://doi.org/10.1016/j.atmosenv.2023.119757, 2023b.
- 1092 Xu, Z. F., Han, Y., Tam, C. Y., Yang, Z. L., and Fu, C. B.: Bias-corrected CMIP6 global dataset for
- dynamical downscaling of the historical and future climate (1979-2100), Scientific Data, 8,
- http://doi.org/10.1038/s41597-021-01079-3, 2021.
- 1095 Yamaguchi, M. and Maeda, S.: Slowdown of Typhoon Translation Speeds in Mid-latitudes in September
- 1096 Influenced by the Pacific Decadal Oscillation and Global Warming, Journal of the Meteorological
- 1097 Society of Japan, 98, 1321-1334, http://doi.org/10.2151/jmsj.2020-068, 2020.
- 1098 Yan, D., Jin, Z. P., Zhou, Y. T., Li, M. M., Zhang, Z. H., Wang, T. J., Zhuang, B. L., Li, S., and Xie, M.:
- 1099 Anthropogenically and meteorologically modulated summertime ozone trends and their health

- implications since China's clean air actions, Environmental Pollution, 343, http://doi.org/10.1016/j.envpol.2023.123234, 2024.
- 1102 Yang, J. X., Lau, A. K. H., Fung, J. C. H., Zhou, W., and Wenig, M.: An air pollution episode and its
- formation mechanism during the tropical cyclone Nuri's landfall in a coastal city of south China,
- Atmospheric Environment, 54, 746-753, http://doi.org/10.1016/j.atmosenv.2011.12.023, 2012.
- 1105 Yang, Z. Y., Li, Z. Q., Cheng, F., Lv, Q. C., Li, K., Zhang, T., Zhou, Y. Y., Zhao, B., Xue, W. H., and Wei,
- 1106 J.: Two-decade surface ozone (O₃) pollution in China: Enhanced fine-scale estimations and
- 1107 environmental health implications, Remote Sensing of Environment, 317,
- http://doi.org/10.1016/j.rse.2024.114459, 2025.
- 1109 Yarnal, B.: Synoptic Climatology in Environmental Analysis A Primer, Journal of Preventive Medicine
- Information, 347, 170-180, http://doi.org/10.1016/j.crte.2014.12.002, 1993.
- Illi Zhan, C. C. and Xie, M.: Land use and anthropogenic heat modulate ozone by meteorology: a perspective
- from the Yangtze River Delta region, Atmospheric Chemistry and Physics, 22, 1351-1371,
- http://doi.org/10.5194/acp-22-1351-2022, 2022.
- 1114 Zhan, C. C., Xie, M., Huang, C. W., Liu, J. N., Wang, T. J., Xu, M., Ma, C. Q., Yu, J. W., Jiao, Y. M., Li,
- 1115 M. M., Li, S., Zhuang, B. L., Zhao, M., and Nie, D. Y.: Ozone affected by a succession of four landfall
- 1116 typhoons in the Yangtze River Delta, China: major processes and health impacts, Atmospheric
- 1117 Chemistry and Physics, 20, 13781-13799, http://doi.org/10.5194/acp-20-13781-2020, 2020.
- 1118 Zhan, Y. Z. H., Xie, M., Zhuang, B. L., Gao, D., Zhu, K. G., Lu, H., Wang, T. J., Li, S., Li, M. M., Luo,
- Y., and Zhao, R. Q.: Particle-ozone complex pollution under diverse synoptic weather patterns in the
- Yangtze River Delta region: Synergistic relationships and the effects of meteorology and chemical
- 1121 compositions, Science of the Total Environment, 946, http://doi.org/10.1016/j.scitotenv.2024.174365,
- 1122 2024.
- 1123 Zhang, G., Murakami, H., Knutson, T. R., Mizuta, R., and Yoshida, K.: Tropical cyclone motion in a
- changing climate, Science Advances, 6, http://doi.org/10.1126/sciadv.aaz7610, 2020.
- Zhang, Z. K., Lu, B. Q., Liu, C., Meng, X., Jiang, J. K., Herrmann, H., Chen, J. M., and Li, X.: Nitrate
- pollution deterioration in winter driven by surface ozone increase, Npj Climate and Atmospheric
- Science, 7, http://doi.org/10.1038/s41612-024-00667-5, 2024.
- 1128 Zhao, S. P., Yin, D. Y., Yu, Y., Kang, S. C., Qin, D. H., and Dong, L. X.: PM_{2.5} and O₃ pollution during
- 2015-2019 over 367 Chinese cities: Spatiotemporal variations, meteorological and topographical
- impacts, Environmental Pollution, 264, http://doi.org/10.1016/j.envpol.2020.114694, 2020.